



Ref: AFS-10-0020
Document No. TP3(51199)GLC012610

January 26, 2010

ATTN: Document Control Desk
Director, Spent Fuel Project Office
Office of Nuclear Material Safety and Safeguards
U. S. Nuclear Regulatory Commission
Washington, DC 20555-0001

SUBJECT: Request for Additional Information on TRUPACT-III, Docket No. 71-9305, TAC No. L24403

- Reference:** (1) Letter, Meraj Rahimi, U. S. Nuclear Regulatory Commission, to Gary L. Clark, Packaging Technology, Inc., *Request for Additional Information on TRUPACT-III*, dated March 6, 2008.
- (2) Letter, Todd Sellmer, Washington TRU Solutions, LLC to C. Staab, U. S. Nuclear Regulatory Commission, Same Subject, Letter No. CP:10:01045/UFC:5822.00, dated January 21, 2010.

Dear Sirs:

In response to Reference (1), AREVA Federal Services LLC (AFS) hereby submits the revised application for a Certificate of Compliance (CofC) for the TRUPACT-III shipping package. This Revision 1 replaces the original application in its entirety. Included within this transmittal are six sets of the following documents:

- Safety Analysis Report (SAR). Six paper copies are provided in three ring binders, and one copy is provided on electronic media.
- TRUPACT-III Authorized Methods for Payload Control (TRAMPAC). Six paper copies are provided in three ring binders, and one copy is provided on electronic media.

The electronic copy is contained on one CD-R in an envelope labeled, "TRUPACT-III Docket 71-9305 Electronic Copy of Documents". The CD-R contains the following files:

- TRUPACT-III SAR, Complete, Rev 1.pdf (SAR)
- TRUPACT-III TRAMPAC, Rev 1.pdf (TRAMPAC)

In addition, each document set (including the electronic copy) includes the following electronic media:

- One DVD-R containing finite element analysis files as part of Appendix 2.12.5;
- One DVD-R containing thermal analysis files as part of Appendix 3.5.1.

Therefore, the electronic copy of the submittal contains a total of three discs, and each paper copy contains a total of two discs, in plastic slipsheets in the rear of the binder. A breakdown of the contents of each CD-R and DVD-R is provided in Attachment A to this letter.

NIMSSO1

AREVA Federal Services LLC

1102 Broadway Plaza, Suite 300, Tacoma, WA 98402-3526
Tel.: 253-383-9000 - Fax: 253-383-9002 - www.aveva.com

Specific responses to each NRC Request for Additional Information (RAI) are provided in Attachment B, which include references to the applicable SAR sections. To assist the NRC staff in its review of the revised application, a summary of the changes to the packaging general arrangement drawings is provided in Attachment C.

Included with this revised SAR is an updated analysis that incorporates an update of the emissivity value originally utilized for the thermal evaluation for the hypothetical accident conditions per 10 CFR§71.73(4). In discussions with the NRC, AFS was made aware of this emissivity issue on another application, and made the conscience decision to incorporate this change. The net effect of utilizing the higher emissivity value on the resulting package temperatures is minimal.

Minor editorial revisions have also been made to the TRUPACT-III SAR. Changes in the text are annotated with a vertical bar in the right margin ("|").

As discussed in Reference (2), AFS requests that the review of this revised application and the responses to the RAIs be expedited to support the U.S. Department of Energy's (DOE's) critical mission for clean-up activities at the Savannah River National Laboratory (SRNL) site.

Should you have any questions regarding this submittal, please contact me at (253) 552-1312 or via E-mail (gary.clark@areva.com).

Very Truly Yours,

AREVA Federal Services LLC



Gary L. Clark, P.E.
TRUPACT-III Program Manager

cc: Chris Staab - NRC-NMSS



Attachment A

Contents of Electronic Media

This submission is composed of both paper copies and an electronic copy. The electronic copy is contained within an envelope labeled, "TRUPACT-III Docket 71-9305 Electronic Copy of Documents". The envelope contains three discs as follows:

Title	Media Type:	Contents
TRUPACT-III SAR	CD-R	Three files of the complete text of the submittal: (1) TRUPACT-III SAR, Complete, Rev. 1.pdf (20,684 kb) (600 pages) (2) TRUPACT-III TRAMPAC, Rev. 1.pdf (4,433 kb) (152 pages)
TRUPACT-III SAR Appendix 2.12.5 FEA Files	DVD-R	A disc entitled "App. 2.12.5 FEA Files" containing three subfolders containing structural analysis computer input and output files used in the preparation of the Appendix 2.12.5 FEA analyses. Total size: 2,390 mb
TRUPACT-III SAR Appendix 3.5.1 Thermal Cases	DVD-R	A disc entitled "App 3.5.1 Computer Analysis Results" containing thermal analysis computer input and output files used in preparation of Chapter 3.0 of the SAR. Total size on disc: 570,143 kb

Note also that one copy of each of the last two discs, e.g., "App. 2.12.5 FEA Files" and "App 3.5.1 Computer Analysis Results" are included in each of the six paper copies of the SAR submittal.

**AREVA Federal Services LLC's RESPONSES TO
NRC REQUEST FOR ADDITIONAL INFORMATION**

Model No. TRUPACT-III, Docket No. 71-9305

NRC Request received March 6, 2008

1.0 GENERAL INFORMATION

- 1.1 Describe the impact of punctures on the lower part of the packaging without full coverage of the puncture-resistant plate.

As shown on Section B-B of Sheet 4 drawing, the puncture-resistant plate does not cover the entire length of the packaging all the way to the end. Given the results of the puncture tests, the bar penetrating all the way through the puncture-resistant plate and damaging the outer plate of the CSA, it is possible for the puncture bar to breach the containment boundary if the drop on puncture bar takes place towards the lower part of the packaging without the full coverage of puncture-resistant plate.

Response: As demonstrated by the supplemental full-scale certification testing, a puncture test performed on the subject area of the packaging does not compromise containment. Details are provided in SAR Section 2.7.3.3.6.

- 1.2 **Drawing 51199-SAR, Sheet 4 and 17 of 21:** Clarify the apparent design/drawing discrepancies for the overpack cover closure bolt "protection cup" of the overpack cover, shown in Zone A-8 of Sheet 4 and Zones C-2 and D-2 of Sheet 17.

The protection cup details shown on Sheet 4 appear to be typical for the protection of all 44 lid closure bolts from being subject to side impact shearing loads under the HAC free drops. Figure 2.12.3-31 of the application displays typical contact marks on the closure bolt head and washer, which suggests that bolt heads have been subjected to a large shearing load during the free-drop tests. It's unclear how the protection cup is configured for its intended function, which appears to have failed.

Response: The cups located in the overpack cover are used to provide clearance for the closure bolt heads, allowing the cover to be assembled directly adjacent to the closure lid. A consequence of the design of the cups is that a potential exists for the cups to interfere with the closure bolt heads and/or washers, given sufficient in-plane translation of the overpack cover relative to the closure lid in a HAC free drop. However, as discussed in Section 2.7.8.2 of the application, in spite of the interference between the cups and the closure bolt heads that did occur on CTU-1, the closure lid was leak tight with only a relatively trivial bolt preload in place, as long as the seal was clean from any internal debris. For this reason, the debris shield has been included in the design. A supplemental certification test (using a new full-scale test unit, CTU-2, which includes the debris shield) using the worst-case free drop and puncture orientation has been performed to confirm the ability of the TRUPACT-III to remain leak tight in the absence of debris on the containment seal. The results of the test are given in SAR Section 2.7.1.4.5 and Section 2.7.8. In addition to adding the debris shield, tolerances on dimensions which affect the fit-up of the overpack cover have been tightened (as

reflected in the Revision 1 SAR drawings) to further limit the potential for interference between the cups and closure bolt heads.

- 1.3 **Drawing 51199-SAR, Sheet 4 of 21:** Clarify the drawing shown in Zone C-4 and Zone C-5 with regards to Item 68 (porous polyurethane filter) to show how the item fits into other surrounding parts.

The debris shield design shown on Zone B-7 with an enlarged drawing shown in Zone C-4 and C-5 lacks in clarity. With only one cross-section shown, it is not clear how the filter of 5/16 inch in diameter and one inch in thickness fits into the drawing (e.g., with a gap present, how does Item 66 connect to Item 68?). Exploded cross-sections from other directions and isometric view should be provided to show the correct configuration and detailed layout.

Response: The view referenced in the question is a cross section of the filter (Item 68). The filter has the shape of a cylinder, 5/16 inches in diameter, with a length equal to the thickness of the closure lid shear lip. A view has been added to Sheet 14, Zone A-2, to more clearly show the configuration of the filter, and the detail shown in Zone C-4/C-5 of sheet 4 has been redrawn.

- 1.4 **Drawing 5119-SAR, Sheets 1 and 19 of 21:** Correct drawing and/or Bill of Materials on Item 65 so that the dimensions of the part (steel bar or receptacle) are consistent between the two sheets.

Drawing Sheet 19, Zone A-4, depicts the dimensions of the receptacle to be 38 mm by 29.5 mm. However, the Bill of Materials on Sheet 1, Item 65 shows that the steel bar has a cross-section of 27 mm by 39 mm. The discrepancies between the two should be resolved by correcting either one or both to bring the dimensions into agreement.

Response: Drawing Sheet 19, Zone A-4 shows the receptacle as 26 × 38 mm. In the list of materials, the item dimensions may be thought of as a suggested stock size for fabrication of the item. They generally show a slightly larger size than the finished item, as appropriate for purchase by a fabricator for machining. Therefore the item 65 description in the List of Materials of 27 × 39 mm is correct.

- 1.5 **Drawing 5119, Sheets 5 and 6 of 21:** Verify the polyurethane foam thicknesses specified for the side and close-end faces of the packaging body assembly.

Drawing Sheet 6 depicts a foam thickness of 114 mm, which is different from the 109 mm identified in Sheet 5 and Figures 1.1.3 and 1.1.6 of the application, and all those thicknesses are different from the 120 mm called out in Section 3.7.3.2 for the sidewalls of the packaging. Also, the 120 mm thick foam identified for the closed-end face deviates from the 140 mm foam thickness described in Section 3.7.3.2.

Response: These dimensions refer to the thickness of the light-density polyurethane foam which forms the inner layer of the puncture-resistant construction on the sides, top/bottom, and ends of the package. On the two sides, the light-density (0.10 kg/dm³) foam is 114 mm thick, as shown in Section G-G on drawing sheet 6. On the top/bottom walls, the thickness is 109 mm, as shown in Section F-F on drawing sheet 5. On the closed end and in the overpack cover, the light-density foam is 120 mm thick, as shown in Section F-F on

drawing sheet 5, and in Section AE-AE on drawing sheet 17. Figure 1.1-3 is a generic figure that shows the range of thicknesses in the four walls (109 mm - 114 mm). Figure 1.1-6 is a side view showing the thickness of the foam specifically in the top wall.

Section 2.7.3.2 (not 3.7.3.2) has been clarified to better describe the foam thicknesses. The 140 mm thickness refers to the medium-density (0.16 kg/dm^3) foam which is located at the outside extremity of the rear overpack face (Section AU-AU on drawing sheet 8) and front cheeks and overpack cover face (Section AE-AE on drawing sheet 17).

2.0 STRUCTURAL

Section 2.2.2 Chemical, Galvanic or Other Reactions

- 2.1 **Page 2.2-3, Material Property for Silicon Foam:** Provide data or assurance for silicon foam used as the insert in the debris shield new design to be free of chemical, galvanic or other reactions.

The major materials of construction of the TRUPACT-III packaging such as stainless steel, alloy steel, copper alloy, polyurethane foam, balsa wood, silicate insulation board, butyl rubber O-ring seal will not have significant chemical, galvanic or other reactions as they have been previously used, without any incident for transporting radioactive materials of similar payload contents. However, with the new design of a debris shield at the containment boundary, a new material of silicon foam (Item 67) is used for the insert, yet its material properties are unknown. Thus materials property data is needed to assure that there will be no chemical, galvanic, or other reactions during the transport.

Response: The discussion of corrosion with respect to the silicone foam debris shield (item no. 67), the polyethylene filters (item no. 68), and the hard plastic plates (item no. 53) in Section 2.2.2.1 of the SAR has been supplemented.

- 2.2 **Page 2.2-3, Material Property for Polyethylene:** Provide materials property data for the filter in terms of its durability and filtering function. Justify using the pore size of one micrometer for the filter.

In the new design of debris shield, a new component of polyethylene filter of 5/16 inch in diameter, one inch thickness with pore size of one micrometer is proposed to be used for equilibrating pressure. Material data of the polyethylene proposed are requested to determine the reliability and its filtering function. Also, provide justification on using the pore size of one micrometer. The information is relevant to the operation, maintenance, QA, and testing programs.

Response: The passive polyethylene filters were selected as part of the debris shield design to act as a pathway for gas to bypass the silicone foam insert that prevents debris from reaching the main closure lid containment O-ring seal. This bypass function is required to ensure that helium will reach the containment O-ring seal for leakage rate testing, as well as preventing a pressure build-up across the silicone foam insert that might promote movement of debris past the insert. The passive polyethylene filters for this application use the same manufacturer (GenPore, fka General Polymeric) and material as those previously utilized in the TRUPACT-II transportation package (Docket 71-9218) for

the same venting function. The permeable polyethylene material was originally developed by Nuclear Packaging, Inc. (NuPac) in 1985 for venting high integrity containers (HICs) that were approved for shallow-land disposal of Class B and C low-level wastes under 10 CFR 61 at the Hanford, WA and Barnwell, SC burial sites. For the HIC applications, the HICs and the passive vent are required to be designed for a 300 year design life. The passive polyethylene filters were tested while exposed to water, clay soil, and air under various pressure differentials to demonstrate the flow of gas under all conditions. No degradation was noted in the performance of the polyethylene filters for any of the tested conditions. The one micron pore size for the polyethylene material was selected to ensure no soil would pass through the passive vent during the 300 year design life. In the TRUPACT-III application, the one micron pore size prevents any debris from bypassing the silicone foam insert and reaching the containment O-ring seal. The polyethylene material is resistant to chemicals and radiation, and is not corrosive to the duplex stainless steel utilized in the TRUPACT-III package. In addition, the use of eight passive filters provides redundancy since a single passive filter can satisfy the required gas pathway and pressure relieving functions. The manufacturer and part number, which specifically identifies the filter material and configuration, have been added to the drawings in Appendix 1.3.1, *Packaging General Arrangement Drawings* of the application.

- 2.3 **Page 2.2-12, Figure 2.2-1, True Stress-Strain Curves for Alloy UNS S31803 and Type 304 Stainless Steel:** Correct the typographic error in the first line of the insert of the figure to read “UNS S31803,” instead of “UNS S31830.”

Response: This typographical error has been corrected.

- 2.4 **Tables in Pages 2.7-14 and 2.7-16:** Delete items relating to red wood in the tables. Since the packaging does not use red wood at all, the information is irrelevant. They should be deleted.

Response: The reference to redwood and the applicable data in the references are pertinent. This section uses results from the half-scale engineering test of the c.g.-over-corner 9m free drop to evaluate the maximum crush in full-scale c.g.-over-corner free drop that would be obtained at maximum temperature. Since the half-scale engineering test unit used redwood, it is necessary to include these properties in the evaluation.

Section 2.5.2 Tie-Down Devices

- 2.5 **Section 2.5.2:** Discuss how the SLB2 is to be stowed in the CSA cavity in order to meet the intent of the 10 CFR 71.45(b) (1) requirements.

It is not clear how spacers, if any, are used to fill the nominal axial gap of about 2 inches between the 2,790-mm long inner cavity of the packaging and the 2,747-mm long SLB2, which rests on the roller floor shown in Figure 2.8.2-1 of the TRAMPAC. If there are no spacers or the SLB2 is unsecured, the resulting fatigue effects on key structural components from the repeated impact of the payload on the CSA closure lid should be evaluated.

Response: The SLB2 payload container is placed inside the TRUPACT-III by means of a payload loading system such as a roller floor, in which the rollers are actuated by air pressure.

When air pressure is applied to the system, the roller assemblies extend above the floor; when the container is in place, the air pressure is released, and the rollers retract, allowing the pallet and container to rest securely on the roller floor upper surface. Thus, the container is not permitted to move back and forth under transport motions (stops, starts, bumps, etc.) on free turning rollers, but is retained in position by the weight of the contents and the friction of the surfaces. This will be true of any payload loading system used in the TRUPACT-III. Thus, no repetitive impact with the containment will occur and fatigue of the closure due to such impacts is not of concern. In addition, the axial gap between the payload cavity and the SLB2 length has been reduced as described in the response to RAI No. 2.8.

Section 2.6.1.3 Stress Calculations

- 2.6 **Page 2.6-4, Stress Analysis of the Governing CSA Wall:** Reevaluate margins of safety for the fillet welds connecting the V-stiffeners to the CSA inner wall for all applicable loading and load combination conditions in accordance with the ASME Code, Division 1, Subsection NB-1132.1 containment boundary jurisdiction provisions.

The fillet welds connecting the load-bearing V-stiffeners, as attachments to the containment boundary, fall within the containment jurisdiction boundary. Section 2.1.4 of the application notes that these welds do not qualify as Subsection NB weld types. Section 2.3.2 further states, "[W]elds that are part of the CSA but not part of the containment boundary are inspected ..., omitting the radiographic inspection." Therefore, appropriate quality factors commensurate with weld inspection procedures must be considered in determining the stress allowables and corresponding margins of safety for all loading conditions, including fatigue, for the subject welds.

Response: AFS agrees that the subject welds belong within the ASME Code, Division 1, Subsection NB jurisdictional boundary, defined as "attachment to components". NB-3123.2 permits welded attachments if a fatigue analysis is performed. Quality factors are not used in Section NB.

Section 2.1.4 of the SAR has been revised to include the V-stiffener fillet welds under the NB classification. The SAR has also been revised to include a fatigue analysis of the fillet weld of the V-stiffener to the containment boundary for the design pressure cycle, see Section 2.6.1.3, *Stress Calculations*. The SAR already considers fatigue of the CSA floor and plug welds under transportation vibration conditions in Section 2.6.5, *Vibration*.

Section 2.6.1.6 Closure Bolts

- 2.7 **Page 2.6-10:** (1) Provide a free-body diagram in the application, including the washer and bolt hole, to illustrate the assumptions used for calculating the stiffness and resulting force in the intervening load bearing structural components. (2) Provide structural performance acceptance criteria and perform an evaluation to demonstrate that the washer over the over-sized bolt hole is adequately sized for preventing the closure bolt from losing its preload functionality as the result of the mechanical impact loads such as those associated with the NCT and HAC free drops.

Page 2-6-10 of the application evaluates stiffness for the closure bolt load path by considering the respective outer and inner diameters of 64 mm and 44 mm for the tube forming the bolt hole in the closure lid. However, it's unclear why the washer stiffness was left out in the evaluation. Section 2.12.3.8.2.2 notes that all bolt washers showed evidence of a thickness reduction due either to the initial preload torque, the applied impact load, or both. Thus, design details and structural acceptance criteria for the closure bolt assembly, including the washer, must properly be captured in the evaluation.

Response: (1) Figure 2.6-2 has been added to Section 2.6 which illustrates the parameters used to calculate k_m , the stiffness of the clamped member (i.e., the closure lid). Since the hardened washer does not experience any yielding under NCT operational loads, the bolting evaluation performed in Section 2.6.1.6 is fully elastic. For this reason, no permanent deformation of the washer occurs, and the evaluations in Section 2.6.1.6 remain valid.

(2) Since the bolt washers experienced a small amount of permanent thickness reduction during the initial testing on CTU-1, the washers have been revised to use a hardenable stainless steel material. During testing of CTU-2, no permanent thickness reduction or distortion of the washers was noted. Furthermore, an evaluation has been added to the SAR (Section 2.7.1.4, supported by the new Appendix 2.12.7, *Closure Lid, Bolt, and Washer Interaction*) to demonstrate that the washers do not experience any permanent deformation under high bolt loads. In addition, this analysis shows that the closure joint experiences less than 10% preload reduction when loaded up to the yield load of the bolt and then released.

Section 2.7.1.2 Certification Test Units and Test Conditions

2.8 **Section 2.7.1.2:** Justify the use of aluminum bars weighing 6,746-kg to provide adequate simulation for the potential dunnage-induced secondary impact effect of a fully loaded SLB2 on the structural and containment performance of the closure lid.

The nominal axial gap of about 2 inches between the 2,790-mm long inner cavity of the packaging and the 2,747-mm long SLB-2, which acts as a whole structural entity, needs to be considered for potential secondary impact effects on the closure lid performance for all applicable drop tests.

Response: To eliminate concern over secondary impacts, the axial free space between the TRUPACT-III and the SLB2 payload container has been reduced to a range of 2 to 28 mm as discussed in SAR Section 1.2.1.1. The maximum gap of 28 mm is achieved by imposing a minimum SLB2 length of 2727 mm (107-3/8 inches) as specified in Section 2.8.1 of the TRUPACT-III TRAMPAC, and by reducing the payload cavity length variation to 2749 to 2755 mm in the region which aligns with the end bumpers on the SLB2. To achieve this, the three 1" x 3" steel guide bars which are used on the sides are now continued across the closed end. Plastic plates of the required thickness are then attached to the closed end guide bars. Because the maximum free space of 28 mm is only 1% of the length of the SLB2, secondary payload impacts are not of concern. Note: the basic length of the package cavity (i.e., from the bolting flange to the rear wall) has not changed.

To ensure that the loading applied by the payload onto the package interior is prototypic during the free drop, the supplementary testing using CTU-2 included a prototypic roller

floor, pallet, and SLB2 container. The SLB2 container was loaded using aluminum bars. Note that, as discussed in SAR Section 2.12.6.3.4, the closed end guide bars and plastic plates were not used on CTU-2, which therefore had a conservatively large axial free space present.

- 2.9 **Section 2.7.1.2:** Justify the use of ambient temperatures in performing the side-edge down (LD5) and C. G.-over-corner (LD4) drop tests given the observed damages to the closure lid/body flange interface, including the plastic offset between the bolt head and the threads which appears to have been associated with the side-impact force on bolt heads.

Results of the LD4 and LD5 tests have demonstrated that damages to the packaging containment capability could have also been associated with high side-impact forces on bolt heads. The staff notes that the crush strength of the energy absorbing materials generally varies inversely with decreased temperature. As such, cold temperature, at -29 °C, other than the prevailing ambient temperature of at least 7 °C, would have resulted in even higher impact forces on the bolt heads.

The package should be tested with appropriate temperature conditions and drop orientations for which maximum damage is expected in accordance with the requirements of 10 CFR 71.73 (b) and (c).

Response: To ensure the worst-case HAC impact test, the supplemental HAC free drop was performed at a temperature in the deformed region of below -29 °C, as discussed in Section 2.7.1.1.3.

Section 2.7.8 Summary of Damage

- 2.10 **Section 2.7.8:** Provide a structural evaluation to show that the closure lid sliding against the CSA body flange is bounded so as not to result in adverse effects on the package performance under the HAC drop accidents.

Page 2.7-36 of the application states, "[I]t is plain that the bolt bending was caused by the side impact on the bolt heads from the overpack cover head recess cups, which struck the heads during a lateral translation of the overpack cover, which in some cases also struck the edge of the washer." In arguing that the condition of the closure bolts and body flanges is of no design concern, Page 2.7-37 further states, "[D]amage to the closure bolts from the single, worst-case free drop and puncture drop would be much less than that which was generated in the certification test series." The staff notes that these statements fail to recognize that the closure lid and its overpack cover are subject to concurrent axial and side impacts in a single C.G.-over-corner HAC drop event, which is likely to result in a loss of bolt preload and would exacerbate the closure lid sliding. As such, bounding damages could be expected from a single C.G.-over-corner drop test, which must appropriately be assessed for the debris shield design consideration.

Response: As shown on the SAR drawing, Flag Note 40, the maximum clearance between the closure lid shear lip and the body opening is 6 mm in the side-to-side or up-down directions. As shown by the results of testing CTU-1, the in-plane motion of the closure lid was successfully controlled by the shear lip within these limits (see Section 2.12.3). CTU-2 was subjected to a HAC free drop in the c.g.-over-corner orientation. As

discussed in Appendix 2.12.6.8.2.1, the in-plane motion of the lid was very small, and despite the fact that the overpack cover cups interfered with several closure bolt washers, no significant bolt preload reduction or any bolt bending was noted. Therefore, the design of the package closure and debris shield is adequate.

Section 2.12.3 Certification Tests

- 2.11 **Page 2.12.3-9:** Clarify the statement, "A hard vacuum would not be obtained between the closure lids, but the internal cavity pressure was maintained."

The statement appears to suggest that the containment continued to remain functional after the last C.G.-over-corner drop test. This is contradictory to the Page 2.12.3-10 assessment, "[T]he leakage rate test of the closure lid containment O-ring seal was, however, not initially successful."

Complete and accurate information should be provided in the application in accordance with the 10 CFR 71.7(a) requirements.

Response: The actual statement in Section 2.12.3.7.5, *CG-Over-Corner, Overpack Cover Down, HAC (Test LD4)*, page 2.12.3-9, is: "A hard vacuum could not be obtained between the closure lid seals, but the internal cavity pressure was maintained." The intent of this statement was to report the exact condition of CTU-1. Maintenance of the internal pressure was not interpreted as a demonstration that containment was maintained. The statement has been revised to read, "A hard vacuum could not be obtained between the closure lid seals, but the leak was not significant enough to have a measureable effect on the internal cavity pressure."

Section 2.12.3.8.2 CTU Measurements

- 2.12 **Section 2.12.3.8.2:** Discuss how the as-built anomaly of body flange surface taper of 0.25 to 0.5 mm over the distance between the inner surface edge and the bolt lines is to be controlled for the production units. Evaluate effect of the taper on the bolt prying force that must be overcome in determining the effective bolt preload for calculating bolt stresses for the closure bolt design.

The observed surface taper suggests a lack of metal-to-metal contact between the closure lid and the body flange. This design or operating condition should be considered in sizing the bolt torque and corresponding bolt preload to ensure adequate closure bolt design.

Response: A taper of only 0.5 mm across a flange which is 140 mm wide is not unexpected for a package as large as the TRUPACT-III. A taper of this general magnitude, and in the same direction, was noted on both CTU-1 and CTU-2. It was noted during post-test inspections of CTU-1 that some galling occurred on the flange face adjacent to the bolt holes. This galling resulted from lateral motion of the closure lid in the presence of high interface forces, which confirms that there was good contact around the bolts. Similar galling was evident on CTU-2, but to a lesser extent, no doubt because CTU-2 experienced fewer free drops and less overall lid sliding. As noted in Appendix 2.12.6.8.2.1, the gap (if any) at the outer edge of the flange joint of CTU-2 did not permit entry of a 0.004-inch thick feeler gauge. Therefore, it is evident that the closure bolts force the closure lid flange to conform to the body flange and provide a tight joint.

The taper is zero at the time the body flange is machined. During the welding of the outer overpack structure to the body, the taper develops. Due to the fact of weld distortion, the taper will be consistent in its direction and magnitude, and has been noted on all three test units, e.g., half-scale test unit, CTU-1, and CTU-2. Therefore, this taper will occur similarly on production units. Since it has been present on all test units and has not been associated with any loss of function, the tapered condition is acceptable for production units.

- 2.13 **Section 2.12.3.8.2:** Explain why the implied overpack crushing/sliding against the closure lid was not identified as a primary cause for the large plastic offset between the head and the threads of the closure bolt given the statements in Page 2.12.3-12: “[T]he worst bolt was No. 17, having a total indicator reading (TIR) of 10.7 mm,” and “[E]ach of the bent bolts also showed evidence of a side impact on the head.”

Causes for closure bolt bending and loss of bolt preloads are not convincingly delineated in the application. The maximum TIR plastic offset of 10.7 mm and the common bolt bending toward the 11:00 o'clock direction appear to be associated primarily with the relative displacements between the overpack and the closure lid during the LD4 C.G.-over-corner drop test for which the lower right center of the packaging landed on the test pad.

Complete and accurate information should be provided in the application in accordance with the 10 CFR 71.7(a) requirements.

Response: In Section 2.7.8.2, *Closure Bolts*, the application stated: "Contact may have occurred in more than one free drop, but most likely the primary case was free drop LD4, the CG-over-corner orientation, based on the direction of bending." Therefore, AFS is in agreement with the NRC staff that the c.g.-over-corner free drop was the most likely cause of the bent bolts, due to relative motion between the overpack cover and the closure bolt heads.

Section 2.12.5 Closure Lid Debris Shield

The following questions on the closure lid/body flange interface damages indicate that failure causes may not have been properly interpreted in the application. This has led to: (1) selecting the two non-causal drop events for determining the debris shield relative motion design criteria, and (2) excluding modeling the most damaging failure mode as related to the bolt head shear impact by the overpack cover during the C.G.-over-corner drop test. RAI No. 2.17 suggests a robust transient impact analysis model for determining debris shield design parameters. However, a more straightforward alternative is retesting of the full-scale test unit with the debris shield in order to demonstrate the performance of the package in maintaining the containment with the debris shield under hypothetical accident conditions in spite of the plastic deformations of the closure bolts.

- 2.14 **Section 2.12.5:** Clarify the statement in Page 2.12.5-3, "...the debris shield must accommodate the relative motions which could occur between the closure lid and the body. These include the lateral position of the lid within the limits established by the shear lip..." by discussing also that the relative motion between the overpack cover and the closure lid could be the primary cause for resulting in large side impact force on the closure bolt head.

As observed in the application, the closure bolts have been shown to bend in opposite direction between the head and threads during the LD4 C.G.-over-corner drop test. This bolt damage

mode would most likely be attributed to the lateral impact on the bolt head by the overpack cover head cups in addition to the interaction between the lid shear lip and the body flange. Results from the CTU tests have provided valuable information on potential closure lid damage modes, and should be considered for evaluating the proposed debris shield design.

Complete and accurate information should be provided in the application in accordance with the 10 CFR 71.7(a) requirements.

Response: The debris shield's purpose is to prevent any small debris particles which may be present inside containment from reaching the containment seal in an impact. It is therefore located wholly within the containment boundary, and needs only to accommodate the relative motion between the closure lid and the body flange. This relative motion is bounded in any lid in-plane direction by the gap between the body flange and the lip on the closure lid. The maximum movement of the closure lid relative to the body flange is not affected by any motions of the overpack cover. While it is acknowledged that the overpack cover can contact the heads of the closure bolts, this has no effect on the conditions existing at the debris shield. The debris shield was included in the supplementary test program described in Appendix 2.12.6 of the SAR, and functioned successfully in keeping debris from the containment seal.

- 2.15 **Page 2.12.5-4:** Justify the consideration of only the lid-down and the flat side down drops in the determination of the bounding axial motions for the debris shield design for which potential secondary impact interactions between the CSA and the SLB2 must also be evaluated in calculating impact responses of the closure lid assembly.

The CTU tests have demonstrated the closure lid capability of maintaining leak-tightness after the sequential lid-down and flat side 9-meter drop tests. This suggests that any credible analysis for evaluating the closure lid/body flange interface performance, including relative motion at the debris shield, must necessarily predict a small gap opening so as not to allow debris to escape from the CSA cavity for these two tests. For this matter, finite element analyses based on these two drop tests should only be used for demonstrating acceptable structural performance of the closure lid, rather than those being reported for determining the debris shield relative motion design criteria.

Response: A discussion has been added to Section 2.7.1.1.3 which demonstrates that the c.g.-over-corner free drop orientation, performed in the cold condition, is the worst case for both the bending of bolts and for a test of the debris shield. This test was performed as documented in Section 2.7.1.4.5 and Section 2.7.8, supported by Appendix 2.12.6. The CTU-2 passed all of the required leakage rate tests, thus demonstrating the performance of the package in the worst-case HAC test conditions.

- 2.16 **Page 2.12.5-4:** Clarify the statement, “[T]he maximum transient dynamic relative motion at the debris shield is calculated to be 3.0 mm. This value will therefore be used as a bounding criterion for axial debris shield function,” to ensure that governing drop test positions are considered for evaluating the proposed debris shield design.

The debris shield relative motion design criteria should be based on the maximum damage expected for the packaging drop accidents. Since the flat side down drop has

been shown to remain leak-tight, it should not be considered as the drop event to drive the debris shield design evaluation.

Response: See the response to RAI Nos. 2.14 and 2.15.

Section 2.12.5.5 Finite Element End Drop Analysis

- 2.17 **Section 2.12.5.5:** Provide benchmarking analysis using the LD4, C.G.-over-corner drop test for evaluating the proposed debris shield relative motion design criteria. Demonstrate that the analysis model, which should also consider the secondary impact effect by the SLB2, is capable of predicting the observed closure lid damage modes, including the bolt head side impact by the overpack cover and the corresponding bolt bending characterized by the permanent offset between the bolt head and threads.

The lid-down drop has been shown to remain leak-tight. As such, it is not a valid candidate for establishing the debris shield relative motion design criteria. Relevant structural damages of the LD4, C.G.-over-corner, drop test, including the bolt permanent offsets, must appropriately be captured in benchmarking the LS-DYNA drop analysis model.

Response: In lieu of a benchmarking analysis, which would be subject to interpretation, AFS has chosen to perform a free drop test in the worst-case orientation as described in Section 2.7.1.1.3 and with results documented in Section 2.7.1.4.5 and Section 2.7.8, supported by Appendix 2.12.6. The CTU-2 passed all of the required leakage rate tests, thus demonstrating the performance of the package in the worst-case HAC test conditions.

Secondary impact conditions were maximized in the supplementary test because the guide bars across the closed end, including the associated plastic plates, were not used in CTU-2. The average clearance between the payload cavity length and the SLB2 length was 57 mm. As discussed in response no. 2.8, the maximum clearance in a production unit will be 28 mm. The supplementary test was therefore conservative.

Section 2.12.5.5 Finite Element Side Drop Analysis

- 2.18 **Section 2.12.5.6:** Apply realistic boundary conditions at the “open” end of the CSA body for the ANSYS quasi-static side-drop flat down analysis to reexamine the calculated body flange rotation of 0.02003 radians and the corresponding relative axial motion of 3 mm between the body flange and the closure lid inner surface.

The side-drop flat down analysis may not have properly been performed. The staff notes that the open end boundary conditions may have resulted in an unrealistically large 3-mm wide gap opening. With the constraints by the closure lid properly incorporated into the ANSYS model, which should be similar to those of the closed end of the CSA body, the calculated gap opening would likely be much smaller than the reported 3 mm. As evidenced in Figure 2.12.5-14, the edge rotation at the “closed” end, shown in Figure 2.12.5-14, is about 0.0045 to 0.0086 radians to result in a maximum gap opening about 1 mm. Consistent with the observation of the LD3 side flat-down drop test, this 1-mm gap opening would not allow the shards or chips at a few millimeter in diameter, shown in Figures 2.12.3-32 and 2.12.3-33, to escape to the seal region to fail the containment O-ring vacuum test.

Complete and accurate information should be provided in the application in accordance with the 10 CFR 71.7(a) requirements.

Response: See the response to RAI No. 2.17.

3.0 THERMAL

- 3.1 **Section 3.1.1.2** Justify centering of the hypothetical waste box within the CSA rather than locating it against the closure lid for maximum heat input to the seals.

A centered hypothetical waste box would not be conservative assumption for maximum heat input the seal regions and may under predict the maximum seal temperature.

Response: The strategy of centering of the hypothetical waste box within the CSA was chosen to yield the maximum payload temperature and, thus, the highest level of CSA pressurization for a given decay heat loading. The justification for maintaining this strategy in terms of the seal temperature is provided by the facts that no direct contact occurs for the nominal SLB2 waste container placement within the package and that even if direct contact were to occur, it would occur only along the 'bumpers' on the SLB container. These 1-1/2 inch square hollow tubes around the side of the SLB2 container (see SAR Figure 3.1-5) will effectively maintain an air gap between the SLB2 container and the lid.

Further justification is provided by the temperatures in Table 3.1-1 which show that the maximum sidewall temperature of the SLB2 box is 62.3 °C. This maximum temperature occurs where the hypothetical waste box is touching the SLB2 container sidewall and, as such, represents the maximum temperature the CSA lid could reach under the scenario where the hypothetical waste box is located against the forward SLB2 container wall and the SLB2 container is allowed to slide against the CSA lid. Even in this extreme event, contact with the CSA lid will act to lower the temperature level within both the SLB2 container and the waste box such that the actual peak lid temperature would be between 62.3 °C and the 52.6 °C reported in Table 3.1-1 for the containment seal. In any case, the maximum seal temperature would still remain well below its established 107 °C temperature limit for NCT conditions.

A similar situation would exist under HAC conditions, with the added non-conservatism that the closer coupling of the hypothetical waste box with the CSA lid structure would act to slightly increase the effective thermal mass in the vicinity of the lid, thus, reducing the ΔT seen for the lid during the HAC transient and yielding a slightly lower peak seal temperature.

A discussion has been added to Section 3.3.1.1, *Maximum NCT Temperatures*, to explain the effect of the hypothetical waste box location on the containment seal temperature.

- 3.2 **Section 3.1.2** Justify the assumption regarding the hypothetical waste box that the decay heat is distributed equally within the payload volume.

It appears that the actual loading of a SLB2 does not have any controls to ensure a uniform heat loading and as such a concentrated heat load in the area seals could be more severe.

Response: The available payload volume is the SLB2 container, not the hypothetical waste box. As stated in Section 3.1.1.2, *Payload Configuration*, the dimensions of the hypothetical waste box were selected to provide a conservative lower bound on the waste stream volume

expected to be transported within a SLB2 container. In fact, since the hypothetical waste box geometry represents 23% of the total waste volume available within the SLB2, the assumed concentration of the decay heat loading within the hypothetical waste box actually represents a non-uniform heat distribution within the SLB2 container. When combined with the conservative assumption that the thermal conductivity of the entire SLB2 payload volume is equal to air, the SAR modeling approach is expected to bound the peak payload temperature for any credible decay heat distribution within the SLB2 container based on an even greater non-uniform decay heat distribution and the actual payload thermal conductivity.

SAR sections 3.1.1.2 and 3.1.2, *Content's Decay Heat*, have been modified to add the above clarifications.

Section 3.1.3 Summary Table of Temperatures

- 3.3 **Page 3.1-5** Substantiate the statement “a small region of the CSA structural sheet may experience embrittlement due to being heated above 316 °C during the HAC fire...”

Page 3.1-5 of the application stated that "a small region of the CSA structural sheet may experience embrittlement due to being heat above 316 °C during the HAC fire..."

However, it is well-known that the stainless steel, UNS S38103 should not undergo reduction of ductility in the temperature range considered. Accordingly, mechanical data are needed to substantiate the statement that, indeed, at 316 °C the material does exhibit embrittlement phenomenon.

Response: The SAR statement simply addressed the possibility of a loss in ductility in a small region of the CSA structural sheet since the predicted peak temperature under HAC conditions exceeded the long-term temperature limit of 316 °C. The SAR conclusions have been revised in light of additional considerations presented in the following paragraphs.

A substantial reduction of ductility in duplex (i.e., UNS 31803) stainless steels when held for sufficient time at elevated temperatures is a well known phenomenon. The onset of this behavior commonly accelerates at 475 °C, thus the term '475 °C embrittlement'. One example in the literature on this subject is *The High-Temperature and Low-Temperature Aging Embrittlement in a 2205 Duplex Stainless Steel*, by Kuang Liang Weng, Tung Hung Chen, and Jer Ren Yang, Bulletin of the College of Engineering, N.T.U., No. 89, October 2003, pp. 45–61. Figure 8 of this paper indicates that aging times in excess of one hour at 725 °C and 11 hours at 650 °C are required to transition from ductile to brittle fracture. These time periods are longer than the entire time the peak CSA structural sheet temperature is above 650 °C during the HAC transient. As such, while a reduction in ductility may occur for the section of the CSA structural sheet affected by the elevated temperature, full embrittlement of the CSA steel is not expected to occur due to insufficient aging time at temperature. In addition, since the maximum temperature of the CSA containment sheets equals 222 °C (which is well below the continuous-use temperature of the steel of 316 °C), no reduction of ductility of the containment sheets will occur.

The significance of possible embrittlement is further reduced by the fact that the fire test is the last hypothetical accident condition which is applicable per 10 CFR 71 (i.e., no post-fire drop events are considered plausible). As such, the only subsequent structural loads occurring for the package will arise from recovery operations. Therefore, even if

reduction in ductility does occur over the small portion of the structural shell affected by the puncture bar damage, no safety impact will result since sufficient package strength will remain to allow recovery operations.

The SAR statement has been revised in light of the above discussion. Section 3.2.2 of the SAR has been revised to include a footnote referencing the above technical paper and to include the discussion above. As noted above, the 316 °C temperature limit for the UNS S31803 material given in Table 3.1-1 is equal to the continuous-use temperature limit (i.e., the maximum temperature listed for the material in Code Case N-635-1) and not the embrittlement temperature. Section 3.4.3.1, *Maximum HAC Temperatures*, has been revised to clarify this point and to further address the embrittlement topic.

A copy of the paper is provided with this submittal.

- 3.4 **Page 2.12.2-3** Revise the temperature range and re-calculate the O-ring compression to assure leak-tight condition under NCT.

The test results in Sec. 2.12.2.6 showed the calculated O-ring compressions over the temperature range of -29 °C to 204 °C. It was concluded that at the minimum temperature of -29 °C the O-ring compression is 18.5%, enough to ensure the leak-tight condition. However, the temperature of the O-ring at center disk can go down to -40 °C (see Table 2.12.2-1) under NCT.

Calculations should be based on this regulated temperature range per 10 CFR71.71 (c)(2).

Response: Section 2.12.2.6, *Test Results*, has been revised to account for the minimum temperature of -40 °C.

- 3.5 **Section 3.2.1** Describe how the thermal conductivity of the exposed balsa wood for HAC is utilized once the temperature of the wood exceeds its allowable temperature limit and its flammability point.

During the hypothetical fire it does not seem reasonable to assume a thermal conductivity for the exposed balsa wood resulting from drop testing, since it would be consumed in the fire. The applicant needs to explain under what conditions this HAC thermal conductivity for the balsa wood was employed and how exposed balsa wood was modeled.

Response: Section 3.5.2.6, *Description of Thermal Model for HAC Conditions*, describes the thermal performance of the balsa wood under HAC conditions and the modeling assumptions applied to the balsa wood. These assumptions can be summarized as wood covered by un-breached sheetmetal will char but not burn, while areas with exposed wood are conservatively assumed to have the wood consumed at the start of the fire. With the exception of the puncture bar damage area, the balsa wood is predicted to remain within sheetmetal encasements with no or only limited exposure to the ambient via weld failures. Under this level of exposure, the balsa wood may char along its exposed surfaces, but will not burn. Further, given that the balsa wood is under laid by a solid metal plate and polyurethane foam, any minor heat generation from wood charring/combustion will not reach the package. Since the thermal conductivity of un-burned balsa exceeds that of charred wood, using the HAC thermal conductivity for wood is conservative for simulating the heat transfer through charred wood.

Where the balsa wood is fully exposed, such as under the puncture bar damage area, the wood is assumed to be gone at the start of the HAC fire, thus exposing the underlying structure to the HAC environment. During the fire, the edges of the exposed balsa are assumed to have receded from the edges of the hole torn in the outer sheet metal of the package from the puncture bar attack. However, the depth of the recession will be self-limiting by the insulating effect of the developed char layer and the package will continue to be protected by the underlying sheetmetal and polyurethane foam.

A reference to Section 3.5.2.6 has been added to Section 3.2.1, *Material Properties*, and clarifying text has been added to Section 3.5.2.6.

- 3.6 **Section 3.2.1** Change the title of Table 3.2.10 to indicate that the radiative properties listed are for NCT.

The SAR text indicates that the radiative properties listed in the subject table are for NCT and the requested change would make the table consistent with the text and avoid any confusion with the thermal properties associated with the hypothetical accident fire. 10 CFR 71.73(c)(4) lists the thermal properties of the package during the HAC fire.

Response: The table title has been changed.

- 3.7 **Section 3.3.1.1** Quantify the effect of assuming no air gaps between component interfaces with foam, balsa wood, or calcium silicate on the maximum NCT package temperatures or minimizing their thickness.

The SAR states that the package temperature levels are driven primarily by the ambient conditions rather than the decay heat. Therefore, any increased thermal resistance from the gaps would tend to lower the temperature in the seal area, which would under predict the maximum NCT temperatures.

Response: The presence of small air gaps between the individual package components is virtually assured by the layered assembly of the package. However, to assess the effect of no air gaps between the component interfaces, the various air gap conductors within the thermal model for NCT conditions were converted to direct contact conductors and the NCT evaluation repeated. As expected, the resulting peak temperatures decreased, but by less than 1 °C. A discussion of this sensitivity analysis has been added to Section 3.3.1.1, *Maximum NCT Temperatures*.

- 3.8 **Section 3.4.1** Describe the consequences of damage to the package if a much longer puncture bar was used (at least equivalent to the width of the package) and the package was dropped in an orientation to produce the maximum damage in an area adjacent to the containment seal. Also, if the damage is more severe than previously analyzed for the HAC fire, then evaluate its effects.

The length of the puncture bar utilized was relatively short compared to the width of the package and it isn't apparent that the package impact with the ground doesn't limit the damage.

Response: This question has two parts: a) what would be the effect of a longer puncture bar, and b) what would be the effect of using a longer puncture bar for the puncture attack adjacent to the containment seal?

- a) The video record of the puncture event on the package sidewall (designated LP1) shows that the package comes essentially to rest before beginning a relatively slow rotation off of the puncture bar. It is clear that the package does not receive any support from the ground before the energy of the 1-m free fall has been absorbed in the wall overpack/puncture-resistant structure. As the package rolled off of the bar, the package c.g. moved away from the bar axis, and the bar bent over. Once the bar begins to bend, the amount of damage to the package has reached its limit. This is also demonstrated in the video, where it is shown that no damage is occurring to the package as the bar bends. Therefore, a longer bar would tend to do less damage rather than more since it would tend to bend sooner due to its longer moment arm. For these reasons, a longer bar would have no effect on the puncture damage experienced in LP1. Review of the other punctures confirms that this conclusion is universally true of the puncture drop tests performed.
- b) The above response demonstrates that a longer puncture bar would not have generated greater damage. In addition, as shown in Section 2.7.3.1, paragraph A, "Puncture on the Side", the LP1 puncture test was performed at an oblique angle through the package's center of gravity to ensure that all of the energy from the 1m free fall was absorbed in the package structures and not partially dissipated via rotation of the package about the puncture bar impact point. Therefore, an actual puncture attack in the region of the containment seal would have exhibited less damage than seen for the LP1 puncture test, partly because the overpack wall structures are stiffer in the region of the containment seals, and partly because the axis of the puncture bar would necessarily not pass through the c.g. of the package. In order for the puncture bar attack to pass through the package c.g., the package orientation would need to be on the order of 55° to the horizontal. An attack at such a steep angle would cause the puncture bar to either glance off of the surface, or simply bend out of the way. Therefore, the observed damage resulting from the LP1 puncture bar attack is bounding for the damage that could be obtained by a similar puncture bar attack elsewhere on the side surface of the package and, as such, the simple transfer of the observed LP1 damage over to the containment seal region provides a significant level of conservatism for the assumed HAC damage scenario for the containment seals.

The details of the damage basis assumed for the fire event is more thoroughly described in Section 3.5.2.6, *Description of Thermal Model for HAC Conditions*, and Section 3.5.3, *Review of TRUPACT-III Package Full-Scale Drop Test Results*.

- 3.9 **Section 3.4.2.** Describe in detail and via illustration, the thermal model utilized (including boundary conditions) for the damaged areas resulting from the drop tests.

The information presented does not include a detailed description of the model used for the damaged areas of the package. Include an explanation of how the exposed balsa wood is considered both during and after the fire.

Response: Appendix 3.5.2.6, *Description of Thermal Model for HAC Conditions*, provides the details of the thermal model used to simulate the damaged package for HAC conditions. The boundary conditions are described in Section 3.4.2, *Fire Test Conditions*. The response to RAI No. 3.5 describes how the exposed sections of balsa are treated during and after the fire.

- 3.10 **Section 3.4.2.** Justify not eliminating the air gaps or minimizing their thickness between component interfaces with foam, calcium silicate, or balsa wood inner surface on the maximum HAC package temperatures.

The SAR states that only the air gap between the outer skin and the balsa wood was assumed to be direct contact. Keeping the gaps from the NCT model would tend to lower the temperature in the seal area, which would under predict their maximum HAC temperature.

Response: The HAC evaluation did eliminate the assumed air gaps between the foam and balsa components of the package sidewall. Section 3.4.2 has been modified to clarify this point. Further, as demonstrated by the sensitivity evaluation conducted for the NCT conditions (see the response to RAI #3.7), eliminating the air gaps had a thermally insignificant effect on the NCT results (i.e., less than 1 °C). This fact, combined with the fact that the peak CSA temperature occurs at the location of the puncture bar damage where the surface of the CSA is directly exposed to the HAC environment and not at locations that underlie the other model segments, demonstrates that presence or absence of the assumed air gaps do not have a significant effect on the maximum HAC package temperature.

A discussion of the effect of the presence or absence of air gaps have on the HAC results has been added to Section 3.4.3.1, *Maximum HAC Temperatures*.

- 3.11 Explain and justify why the CSA stiffeners don't conduct and radiate heat to produce a higher localized temperature than 150 °C on the containment sheet of the CSA as shown on Figure 3.4-1 "Temperature Response of TRUPACT-III Package to HAC Fire Event," when the corresponding structural sheet that is only 124 mm away is at 714 °C.

Response: Conductive heat transfer within the CSA structure is limited by the spacing and size of the stiffeners (i.e., 4 mm) and the thermal conductivity of the UNS S31803 stainless steel. The stiffeners also block direct radiation exchange between the inner and outer sheets of the CSA structure. When combined with the relatively low emissivity of the stainless steel surfaces, the presence of the stiffeners significantly reduces the principal heat transfer mechanism during the high temperature HAC event. Additionally, it should be noted that the referenced temperature difference occurs during a transient event. The temperature difference would be much smaller for steady-state conditions.

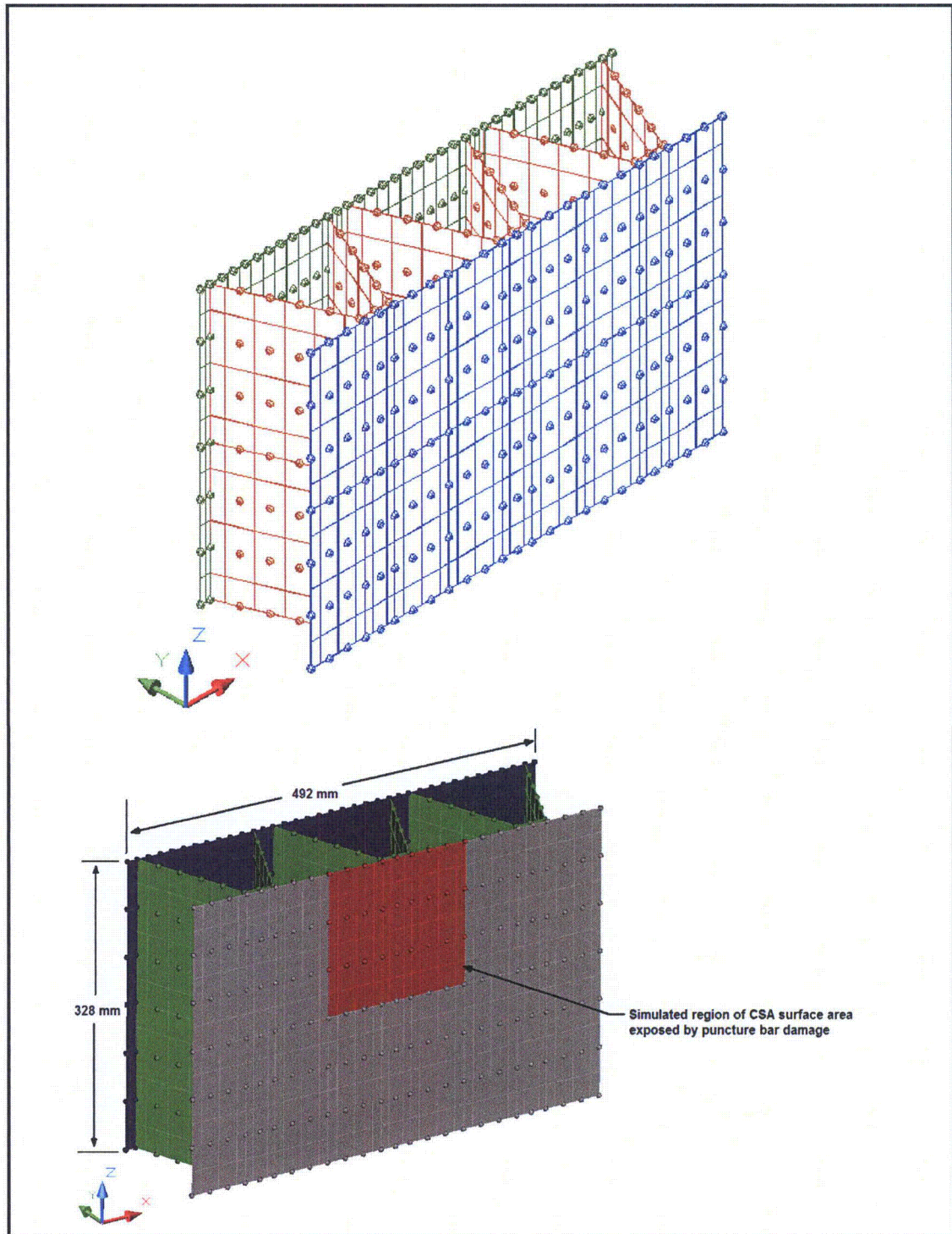
In responding to this comment, it was noted that the predicted peak structural sheet temperature of 714 °C exceeded the temperature range of the effective thermal properties for the corrugated wall structure previously presented in Table 3.2-2. As such, the previous HAC thermal model did not fully capture the non-linear effect of temperature during the HAC event. To correct this, the effective thermal properties were extended (see revised Table 3.2-2) to a bounding temperature range and the HAC thermal evaluation repeated. The resultant peak CSA containment sheet temperature increased from 151 to 222 °C, while the peak CSA structural sheet temperature decreased from 714 to 689 °C due to the higher heat transfer rate between the structural and containment sheets.

Verification of the SAR evaluation results is provided through use of an extended version of the thermal model used to establish the effective thermal properties of the CSA wall structure (see SAR Appendix 3.5.2.4, *Effective Thermal Properties for Corrugated Wall/Lid Structures*, for a description of the model). This extended thermal model joined six (6) segments of the

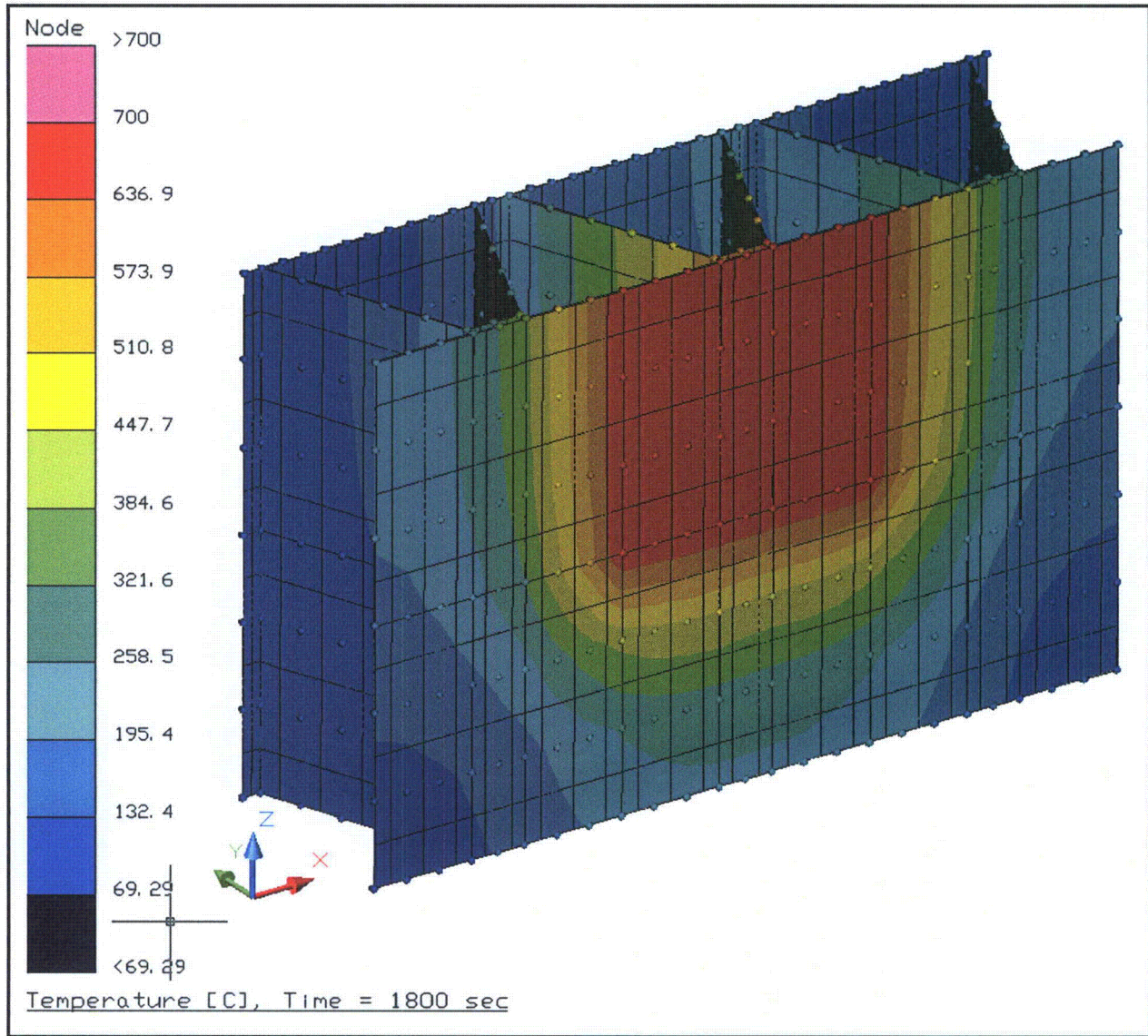
model depicted in Figure 3.5-11 to form a simulated wall segment that is 492 mm wide by 328 mm high. A transient boundary temperature condition that varied from 55 °C at time = 0 to 700 °C at time = 900 sec was applied to the structural sheet of the top, center 164 mm x164 mm sub-segment of the structural wall model to simulate the combined radiative and convective heating on a limited portion of the CSA's surface during the HAC event due to damage caused by the puncture bar attack. The proportion of the sub-segment to its neighboring segments is similar to the portion of the CSA surface exposed by the puncture bar attack.

The 700 °C boundary condition was then maintained for the final 900 seconds of the transient. Adiabatic conditions are assumed on the remaining five (5) segments of the structural sheet to conservatively simulate the limited heat transfer into the polyurethane foam that covers the CSA, while a radiation boundary condition to a 55 °C sink temperature is applied to the containment sheet to simulate the CSA's interaction with the payload cavity.

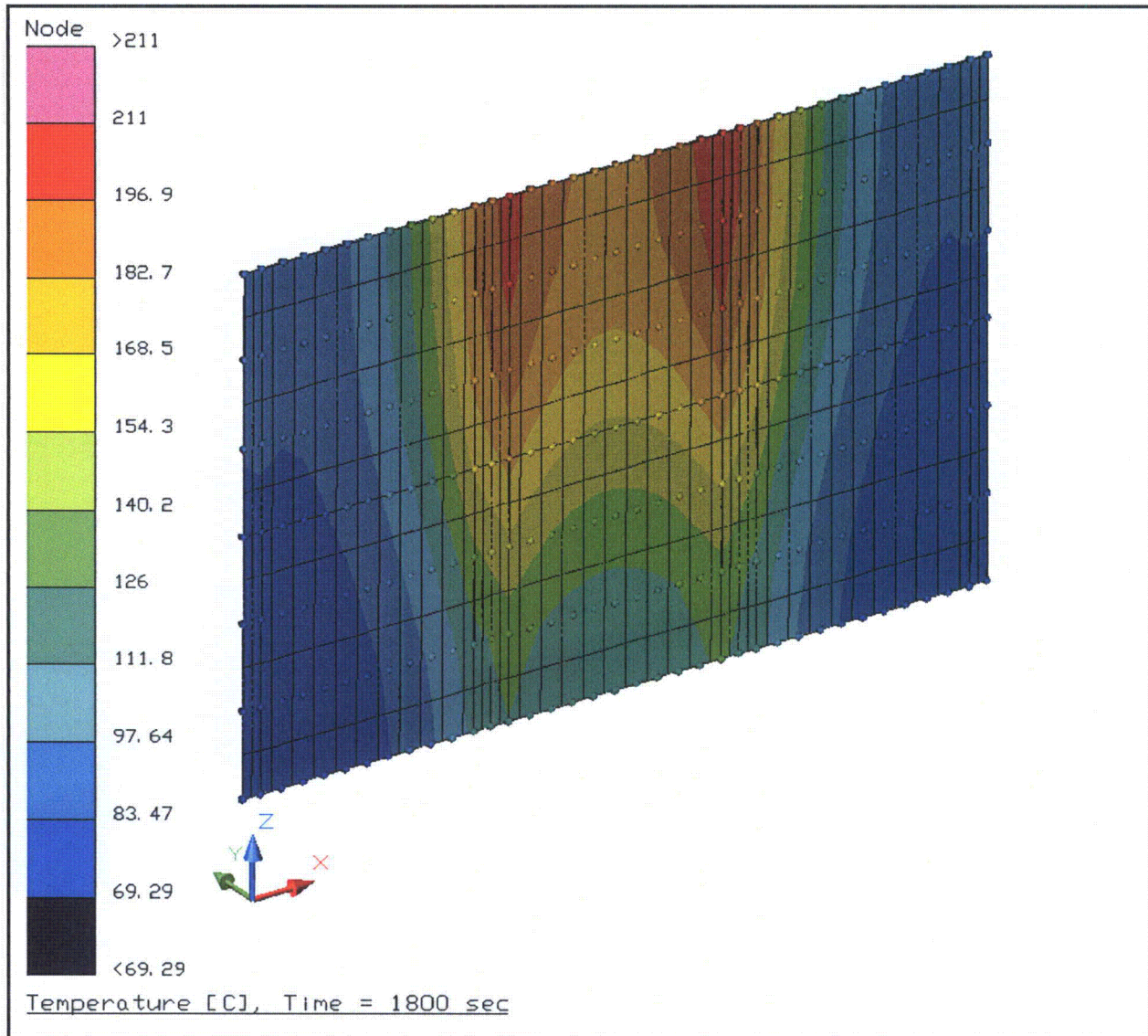
The figures below illustrate the extended thermal model and the temperature distribution within the simulated CSA wall structure at the end of the simulated 30-minute fire transient. As noted from the figures, the peak structural sheet temperature is 700 °C which bounds that predicted by the HAC evaluation, while the predicted peak containment sheet temperature is 211 °C. This predicted peak containment wall temperature level is consistent with that seen by the HAC evaluation of the TRUPACT-III package. An examination of the predicted temperature distribution on the containment sheet demonstrates how the V-stiffeners act to restrict the heat flow into the containment sheet under the transient high heat flux conditions that exist for the portion of the CSA surface exposed by the puncture bar attack.



Layout of Extended Thermal Model for CSA Wall



Temperature Distribution within CSA Wall at End of Simulated 30-Minute Fire Conditions



Temperature Distribution on CSA Containment Wall at End of Simulated 30-Minute Fire Conditions

6.0 CRITICALITY

6.1 **Section 6.2.3** Provide additional justification for using a non-conservative geometry (i.e., pyramid) in your analysis of the reconfigured fuel lump. Alternatively, revise your analysis of reconfigured fuel to adequately bound the unknown configuration of the fuel.

During a fuel reconfiguration there is no definitive way to postulate what ultimate configuration the fuel may assume. Given the wide range of materials that may be compacted, including plastic bags and other items that may be able to hold a somewhat spherical shape of moderated fissile material, assuming a non-conservative shape as the bounding case, necessitates a much more thorough justification.

This information is necessary to ensure compliance with 10 CFR 71.55(b)(1).

Response: The criticality analysis in SAR Chapter 6 has been revised to consider a spherical fissile geometry.

Contact Handled-Transuranic Waste Authorized Methods for Payload Control (CH-TRAMPAC)

Unless otherwise indicated, the following RAls are needed to determine compliance with 10 CFR 71.43(d).

TR-1 Revise the application to compare the TRUPACT-III TRAMPAC to the previously approved CH-TRAMPAC for the TRUPACT-II and HalfPACT packages. Justify any significant differences between the requirements in the CH-TRAMPAC and the TRUPACT-III TRAMPAC.

Given that the TRUPACT-III is designed to transport the same or similar material as the previously approved TRUPACT-II and HalfPACT packages, the payload requirements should also be very similar. Deviations from the previously approved payload requirements should be justified.

Response: Comment incorporated. The TRUPACT-III TRAMPAC document has been revised to specify payload requirements that are the same as those previously approved in the CH-TRAMPAC for the TRUPACT-II and HalfPACT packages. Remaining differences between the authorized payloads for the TRUPACT-III and the TRUPACT-II/HalfPACT are due to packaging design differences and a different payload container type. These are summarized and justified below.

TRUPACT-III TRAMPAC Deviation from CH-TRAMPAC	TRUPACT-III TRAMPAC Section	CH-TRAMPAC Section/CH-TRU Payload Appendix	Justification for Difference
The only authorized payload container for the TRUPACT-III is the Standard Large Box 2 (SLB2).	2.1.1, 2.2.1, 2.8	2.1.1, 2.2.1, 2.9 Appendices 4.1, 4.2, 4.3, 4.4, 4.5	The SLB2 has been specifically designed for the TRUPACT-III. The SLB2 is sized to accommodate the packaging of existing boxes as well as containers of smaller sizes. As stated in TRUPACT-III TRAMPAC Section 1.1, the TRUPACT-III packaging has been designed and developed primarily for the transportation of large boxes.



TRUPACT-III TRAMPAC Deviation from CH-TRAMPAC	TRUPACT-III TRAMPAC Section	CH-TRAMPAC Section/CH-TRU Payload Appendix	Justification for Difference
The TRUPACT-III package does not require the use of dunnage containers to complete a payload.	None	2.2	The SLB2 has been specifically designed for efficient loading of the TRUPACT-III. As a single SLB2 fills the entire TRUPACT-III cavity and comprises the payload, no dunnage containers are necessary to complete the payload.
The TRUPACT-III package does not specify a center of gravity requirement.	None	2.3.1.2	A single SLB2 fills the entire TRUPACT-III cavity and comprises the payload. Similar to the HalfPACT payload, no center of gravity requirement applies to the TRUPACT-III payload.
Machine-compacted waste and greater than 1 percent beryllium (Be) and beryllium oxide (BeO) are prohibited from the TRUPACT-III package.	3.1	3.1	The criticality analysis performed for the TRUPACT-III package did not evaluate the potential presence of machine-compacted wastes or greater than 1 percent Be/BeO-contaminated wastes. Therefore, machine-compacted wastes and greater than 1 percent Be/BeO-contaminated wastes are prohibited from the TRUPACT-III payload.
Solidified organic waste is not an authorized content for the TRUPACT-III.	5.1	5.1	Solidified organic waste is not anticipated in the waste inventory to be transported in the TRUPACT-III.
The TRUPACT-III TRAMPAC does not include alpha-numeric payload shipping categories.	5.1	5.1	The TRUPACT-III TRAMPAC uses only the numeric payload shipping category notation. The alpha-numeric payload shipping category notation described in the CH-TRAMPAC was used only for payload containers that were assigned payload shipping categories prior to the establishment of the numeric notation.
The TRUPACT-III TRAMPAC includes the TRUPACT-III design pressure analysis.	5.4	None	The TRUPACT-III TRAMPAC consolidates the design pressure analysis. Similar analyses for the TRUPACT-II and HalfPACT are presented in the respective packaging safety analysis reports instead of in the CH-TRAMPAC.
The TRUPACT-III payload requirements do not describe mixing of shipping categories.	None	Appendix 2.4	The TRUPACT-III payload consists of only a single payload container (assigned to a single shipping category). As such, mixing of multiple payload shipping categories is not applicable.
The TRUPACT-III payload requirements do not describe 20-day close-proximity shipments.	None	Appendix 3.5	A shipping period of 10 days (with controls) or 60 days (default) will be used for all shipments, as applicable.

TRUPACT-III TRAMPAC Deviation from CH-TRAMPAC	TRUPACT-III TRAMPAC Section	CH-TRAMPAC Section/CH-TRU Payload Appendix	Justification for Difference
The TRUPACT-III payload requirements do not describe overpacking of payload containers.	None	Appendix 6.10	The overpacking concept is not used to describe the TRUPACT-III payload, which is directly packaged in the SLB2 payload container.
The TRUPACT-III payload requirements do not describe shipment of tritium-contaminated waste.	None	Appendix 6.11	Tritium-contaminated waste is not anticipated in the TRUPACT-III waste inventory.
The TRUPACT-III payload requirements do not describe shipment of high-wattage waste under the conditions of CH-TRU Payload Appendix 6.12.	None	Appendix 6.12	The CH-TRU Payload Appendix 6.12 analysis has not been performed for the TRUPACT-III and, as such, the shipment of waste under these conditions is not allowed in the TRUPACT-III.

TR-2 Revise Figure 5.1.2-1 and associated text in the TRUPACT-III TRAMPAC document to clarify that all payload containers to be shipped in the Model No. TRUPACT-III package must meet either the 500 ppm limit on headspace VOC concentration, or the Allowable Flammable Gas Concentration (AFGC).

Figure 5.1.2-1 - Methodology for Compliance with Flammable (Gas/VOC) Concentration Limits, appears to show that waste described by an approved content code is not screened for the 500 ppm headspace VOC concentration. This figure should be revised to show that the flammable VOC criteria should be met by all payload containers, including those for which a content code already exists.

Response: Comment incorporated. TRUPACT-III TRAMPAC Chapter 5.0, Gas Generation Properties Requirements, has been revised to be consistent with the gas generation compliance logic of CH-TRAMPAC Chapter 5.0 (for TRUPACT-II and HalfPACT payloads). New TRUPACT-III TRAMPAC Figures 5.2-1 and 5.2-2 and the associated gas generation compliance logic require all SLB2s to be screened for a total flammable VOC headspace concentration of less than or equal to 500 ppm for compliance evaluation under the analytical category or greater than 500 ppm for compliance evaluation under the test category. As described in TRUPACT-III TRAMPAC Sections 5.2.2.3 and 5.2.2.4, if the SLB2 headspace flammable VOC concentration is greater than 500 ppm, the flammable gas generation rate is calculated using the measured flammable gas concentration and the time history of the SLB2 (based on the methodology in Appendix 3.10 of the CH-TRU Payload Appendices). The flammable gas generation rate is used to calculate the flammable gas concentration within the innermost layer of confinement at the end of the shipping period for evaluation against the Allowable Flammable Gas Concentration (AFGC). This requirement is applied on an individual SLB2 basis irrespective of content code assignment.

TR-3 Revise Section 7.1.1.4 of the TRUPACT–III TRAMPAC document, and associated text in other sections of the document, to list the waste types to be transported in the TRUPACT–III package and their associated flammable gas G values to be used in the determination of decay heat limits.

This section of the TRUPACT–III TRAMPAC, as stated, allows the determination of effective flammable gas G values for each content code by the WIPP CH-TRU Payload Engineer. This appears to be a departure from the compliance methodology for gas generation requirements approved for the TRUPACT-II and HalfPACT packages, where G values were pre-determined for various waste types and applied to content codes containing those waste types.

Response: Comment incorporated. TRUPACT–III TRAMPAC Chapter 5.0, Gas Generation Properties Requirements, and Appendix 8.1.1, Derivation of Flammable Gas Generation Rate Limits and Decay Heat Limits, have been revised to be consistent with the gas generation compliance logic of CH-TRAMPAC Chapter 5.0 (for TRUPACT–II and HalfPACT payloads). The revised logic uses the same waste material types and associated flammable gas G values as the CH-TRAMPAC in the determination of decay heat limits for the SLB2 (with the exception of solidified organic waste, which is not an authorized content for the TRUPACT–III).

TR-4 Revise the TRUPACT–III TRAMPAC to include the requirements for venting and aspiration of payload containers to be transported.

Section 5.2 of the TRUPACT–III TRAMPAC states that unvented containers "shall be aspirated to ensure equilibration of any gases that may have accumulated in the closed container prior to transport." This section does not provide any specific requirements for venting and aspiration of payload containers, as are present in the previously approved CH-TRAMPAC. This section should be revised to include requirements and methods of compliance and verification for ensuring that payload containers are properly aspirated prior to shipment.

Response: Comment incorporated. TRUPACT–III TRAMPAC Section 5.3, Venting and Aspiration, has been revised to include the requirements for venting and aspiration consistent with CH-TRAMPAC Section 5.3. The venting and aspiration requirements are applied to containers stored in an unvented condition to ensure equilibration of any gases that may have accumulated in the closed container prior to transport. As referenced in TRUPACT–III TRAMPAC Section 5.3, containers that have been stored in an unvented condition shall be aspirated for a sufficient period of time that is to be determined using the methodology outlined in Appendix 3.7 of the CH-TRU Payload Appendices.

Chapter 8 ACCEPTANCE TEST and MAINTENANCE PROGRAM

- 8.1 Provide information on polyurethane filter used in the new debris shield design with regards to fabrication, installation, QA, acceptance, operation, and maintenance in the appropriate sections.

In a new design of the debris shield, a filter using polyethylene material with specific specifications is proposed. Yet information on fabrication, installation, QA, acceptance, operation, and maintenance are not provided. Sections involved include, but not limited to: Sec. 2.3: Fabrication and Examination; Sec. 8.1.5: Component Test, and Sec. 8.2: Maintenance Program.

This information should be provided with the application in accordance with the 10 CFR 71.35(a).

Response: Fabrication and installation requirements for the passive filters have been added to the packaging general arrangement drawings in Appendix 1.3.1, *Packaging General Arrangement Drawings* of the application. These additional requirements include the manufacturer and part number, which specifically identifies the filter material and configuration, and the installation requirement (i.e., stake in-place). For maintenance, a new subsection, Section 8.2.5.4, *Passive Filters*, has been added to Section 8.2.5, *Miscellaneous Tests*, to verify the function of the passive filters on an annual basis or when damaged, whichever is sooner. Because the primary function of the passive filter is to prevent a pressure differential across the debris shield, no other maintenance or examination of the passive filter is required to ensure their function as part of the debris shield design.

2205 雙相不銹鋼高溫及低溫時效脆化之研究

THE HIGH-TEMPERATURE AND LOW-TEMPERATURE AGING EMBRITTLEMENT IN A 2205 DUPLEX STAINLESS STEEL

翁光良* 陳東宏† 楊哲人‡

Kuang Liang Weng Tung Hung Chen Jer Ren Yang

*博士班研究生 †博士 ‡教授
國立台灣大學材料科學與工程學系

*Ph.D. candidate †Ph.D. ‡Professor

Institute of Materials Science and Engineering, National Taiwan University, Taipei, Taiwan 10617, R.O.C.

Abstract

The effect of isothermal treatment (at the temperatures ranging between 400 and 975°C) on the embrittlement of a 2205 duplex stainless steel (with 45 ferrite-55 austenite, vol%) has been investigated. The impact toughness and hardness of the aged specimens were measured, while the corresponding microstructure and fractography were studied. The results indicated that the impact toughness of duplex stainless steel was sensitive to the precipitation of σ phase even at the initial stage of high temperature aging. Two kinds of Cr-, Mo-enriched intermetallic phases, σ and χ , were found to precipitate preferentially at δ/γ interface and within δ -ferrite grain after 5 min of aging at the temperature range of 875 ~ 900°C. The volume fraction of σ phase was continuously increased with the time of aging and σ phase developed into a coarse particles due to the high diffusibility of solute atoms at high temperatures. Additionally, the steel is susceptible to severe embrittlement when exposed at 475°C. High-resolution transmission electron microscopy revealed that an isotropic spinodal decomposition occurred during aging at 475°C in the steel studied; the δ -ferrite decomposed into a nanometer-scaled modulated structure with a complex interconnected network, which contained an iron-rich b.c.c. phase (α) and a chromium-enriched b.c.c. phase (α'). It is suggested that the locking of dislocations in the modulated structure leads to the severe embrittlement.

Keywords: Duplex stainless steel; Embrittlement; Impact toughness; Hardness; Spinodal decomposition.

摘要

本實驗係針對已固溶化處理之 2205 雙相不銹鋼 (45% δ , 55% γ , vol%)，於 400 ~ 975°C 溫度區間進行系列的恆溫時效處理，探討雙相不銹鋼在不同時效溫度對脆性的效應及顯微組織隨處理時間變化的情形。由實驗結果顯示：經高溫時效處理，2205 雙相不銹鋼之常溫衝擊韌性對二次相的析出非常敏感，整體的硬度隨析出量的增加而逐漸提高。由金相及顯微組織觀察得知：在 875 ~ 900°C 的高溫時效期間內，有兩種富 Cr、Mo 之介金屬二次相， σ 相及 χ 相快速地自雙相介面處析出。其中， σ 相隨時效時間的增加持續析出，發展成粗大的二次相顆粒。伴隨著二次相於介面析出，臨近的 γ 相逐漸往 Cr、Mo 匱乏的 δ 相區域擴展。經過長時間的高溫時效處理，原雙相組織中不穩定的 δ 相將完全分解成 σ 相與 γ 相。另外，在 475°C 時效溫度，肥粒鐵相產生嚴重脆性，由高解析電子顯微鏡觀察結果顯示，肥粒鐵相在 475°C 溫度時效後，產生均向性離相分解，最初肥粒鐵相分解成微細的富鐵 α 相及富鉻的 α' 相，最後形成奈米大小且相互連接的網狀結構，此結構阻礙差排移動，導致材料脆化。

關鍵詞：雙相不銹鋼、脆化、衝擊韌性、硬度、離相分解。

1. INTRODUCTION

Duplex stainless steels have been widely used in oil, chemical and nuclear industries due to their higher strength, better weldability, and higher resistance to

stress corrosion and pitting. The superior properties of the duplex stainless steels come primarily from approximately equivalent amounts of austenite (γ) and δ -ferrite [1]. However, the deterioration in toughness and in corrosion resistance as a result of exposure to

high temperature, which is the case during fabrication, is a typical problem to users of duplex stainless steels. Indeed, the undesirable phases such as intermetallic phases, carbides and nitrides may exist in the steels and profoundly affect their properties if the manufacturing processes are not properly controlled. Among these secondary precipitates, σ phase with fast formation kinetics has been particularly noticed since it can cause a drastic deterioration in toughness and in corrosion resistance [2]. Although some research work on the aging behavior in 2205 duplex stainless steel has been performed [3], the relationship between microstructure and mechanical properties still needs to be further investigated.

On the other hand, it is well known that in Fe-Cr alloys there is a miscibility gap, where the ferrite phase may decompose into an iron-rich b.c.c. phase (α) and a chromium-enriched b.c.c. phase (α') either by nucleation and growth of α' precipitates or by spinodal decomposition [4,5]. The complex chemistry of the original δ -ferrite in the duplex stainless steels would significantly affect the above mentioned phase transformation. Atom probe field ion microscopy has been performed on CF series of cast duplex stainless steels aged at 270 ~ 450°C; and the morphology, size distribution and chemical concentration profile of the α' precipitates have been determined [6-9]. However, a detailed high resolution transmission electron microscopy has not been reported.

The purpose of this work is to investigate the effects of isothermal aging on the embrittlement and the corresponding phase transformation in a 2205 duplex stainless steel. The atomic structure of α' phase in this steel has been observed via a 300kV field-emission-gun transmission electron microscope (FEG-TEM), Tecnai F30.

2. EXPERIMENTAL PROCEDURE

The as-received material was a commercial wrought 2205 duplex stainless steel rod (53mm) produced by Gloria Material Technology Corporation through the fourfolded forging of a cast slab at 1160 ~ 1180°C and annealing at 1050°C for 30min, followed by water quenching. The chemical composition of the alloy is listed in Table 1. In this work, aging treatments in the temperature range of 400 ~ 975°C for various time intervals from 5min to 64h were carried out and the corresponding microstructural features, hardness and toughness were determined. Charpy impact specimens were machined from the half radius positions of the original rod along the longitudinal direction, in the form of a 11 × 11 × 56mm³ bar. After the aging treatments Charpy specimens were machined in the standard 10 × 10 × 55mm³

Table 1 Chemical composition of the 2205 duplex stainless steel studied (wt%)

C	Si	Mn	P	S	Cr	Ni	Mo	N	Fe
0.02	0.38	1.47	0.022	0.001	22.62	5.12	3.24	0.196	Bal

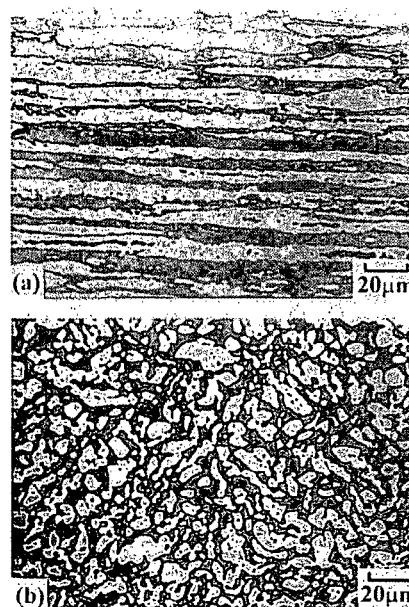


Fig. 1 Optical micrographs of as received steel bar (a) longitudinal section; (b) transverse section

dimensions. Charpy impact tests were carried out at room temperature. The hardness tests were made by using a Rockwell hardness C tester (with a load of 150kg) and a Vickers hardness tester (with a load of 10g).

Fractography of the impact specimens was performed in a Leo 1530 scanning electron microscope (SEM) operated at 15kV. Specimens for optical metallography were prepared from the aged specimens and electrolytically etched in a 32N KOH solution at 9V etching potential for 5s. Transmission electron microscopy specimens were also sliced from the aged specimens, thinned to 0.06mm by abrasion on SiC papers and twin-jet electropolished using a mixture of 5% perchloric acid, 25% glycerol, and 70% ethanol in the temperature range of -5 ~ -10°C and 45V etching potential. The microstructures and microanalyses on the aged specimens were investigated using a JOEL JEM 2000 EX II equipped with an energy-dispersive X-ray spectrometer (EDS). Furthermore, the structural and compositional analyses of sub-nanometer scaled structures were examined using a FEG-TEM Tecnai F30 equipped with nanometer probe EDS.

3. RESULTS AND DISCUSSION

3.1 Impact Toughness and Hardness

3.1.1 Low temperature aging

The optical micrographs shown in Figs. 1(a) and 1(b) were obtained from the as-received 2205 duplex stainless bar studied in this experiment. The structure consists of white etched austenite (γ) islands embedded in a gray etched δ -ferrite matrix with no other secondary precipitates. As a consequence of being deformed in the two-phase region, a banded texture of elongated γ islands is observed on the longitudinal section (Fig. 1(a)), while the more isotropic structure of γ -grain is found on the transverse section (Fig. 1(b)). The volume fraction of γ phase measured by quantitative metallography is about 0.55. Table 2 shows the concentrations of major alloying elements in the δ and γ phases analyzed by EPMA for the as-received specimen. As expected, δ -ferrite is partitioned with the elements of Cr, Mo and Si, while the γ phase contains increasing Ni and Mn contents. Because light elements were not detectable, C and N were not taken into account in these determinations. The measured composition of δ -ferrite is 66.6Fe-23.8Cr-3.86Ni-3.92Mo-1.35Mn-0.44Si (wt%).

Table 2 Chemical composition of the as-received specimen in 2205 duplex stainless steel by EPMA (wt%)

Element	Fe	Cr	Ni	Mo	Mn	Si
δ	66.6	23.8	3.86	3.92	1.35	0.44
γ	68.1	21.2	6.21	2.56	1.63	0.33

Charpy impact toughness was determined at room temperature using three specimens for each combination of aging time and temperature. The results are presented in Fig. 2; it can be seen that the toughness decreases with increasing the aging time. In the cases of aging at 450, 475 and 500°C, a significant decrease in toughness occurs in the initial stage and subsequently an accelerated drop in toughness happens. However, the drop in toughness in the same early stage is negligible in the case of aging at 400°C. For the specimens aged at 475°C for 8h, the impact energy falls to less than half (150J), when compared with the specimens without aging (i.e., An impact energy of the as-received material is 304J). An impact energy of 10 ft-lb (13.5J) is usually considered as a valid criterion for the complete embrittlement condition. For specimens aged at 475°C, it takes 32h to reach this condition; the results are consistent with those obtained from fractographic evaluations. It is evident that aging at 475°C leads to severe deterioration in the toughness of the steel investigated. Figure 3 shows the variation of Rockwell C hardness (HRC) as a function of aging time at different aging temperatures; it indicates that

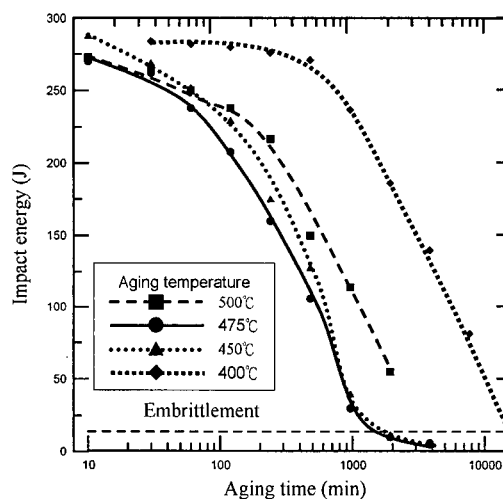


Fig. 2 Effect of aging treatments on Charpy V impact energy of 2205 duplex stainless steel aged at 400 ~ 500°C (Impact energy of as-received material: 304J)

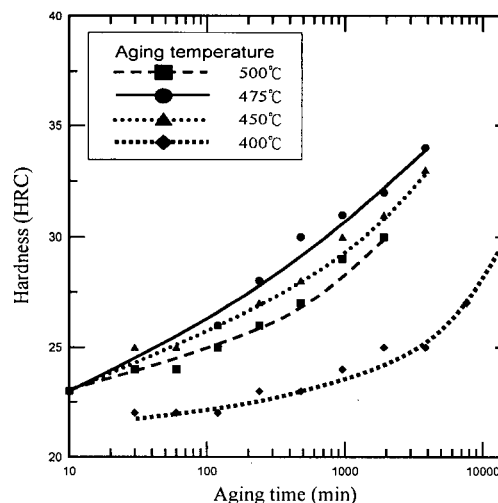


Fig. 3 Effect of aging treatments on HRC macro-hardness of 2205 duplex stainless steel aged at 400 ~ 500°C (Hardness of as-received material: HRC 22)

the hardness increases with increasing aging time at all temperatures except for the initial stage of the aging at 400°C. This result indicates that the embrittlement phenomenon is accompanied by an increase in hardness. Figure 4 is a plot of Vickers hardness versus aging time for different aging temperatures; the data suggests that the embrittlement in the steel is mainly associated with the aging hardening of δ -ferrite. However, the corresponding optical metallographs can not reveal any clear changes in microstructure during the stages of aging.

Scanning electron micrographs at a low magnification (Fig. 5) show detailed fracture morphologies from the center regions of the fracture surfaces from Charpy impact specimens aged at 475°C for different aging times. In the early stages of aging, the ductile fracture mechanism is dominant as shown in Figs. 5(a) and 5(b), where a large number of deep dimples can be observed. After an aging time of 8h, the fracture appearance (Fig. 5(c)) reveals small and poorly defined facets connected by tear ridges or shallow dimples; within the facets, a slight river pattern can be seen radiating from the facet center. In the specimen aged at 475°C for 16h (Fig. 5(d)), a typical river pattern can be observed. The fracture surface of specimens aged at 475°C for 32h and 64h (Fig. 5(e) and 5(f)) show predominant quasi-cleavage areas, suggesting that the brittle fracture mechanism has become dominant. From the fractographic observations, it is apparent that a drastic drop in toughness is connected with the embrittlement and cleavage of δ -ferrite. Apparently the δ -ferrite is prone to brittle failure upon aging. The increased brittleness of the continuous δ -ferrite phase in the matrix has a strong influence on the fracture mode of the austenite, which changes from dimple rupture to tearing rupture [10].

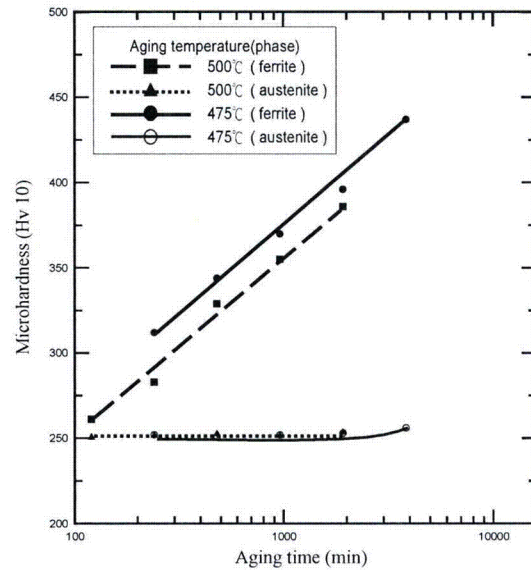


Fig. 4 Effect of aging treatments on Vickers microhardness of δ -ferrite and austenite for different aging temperatures

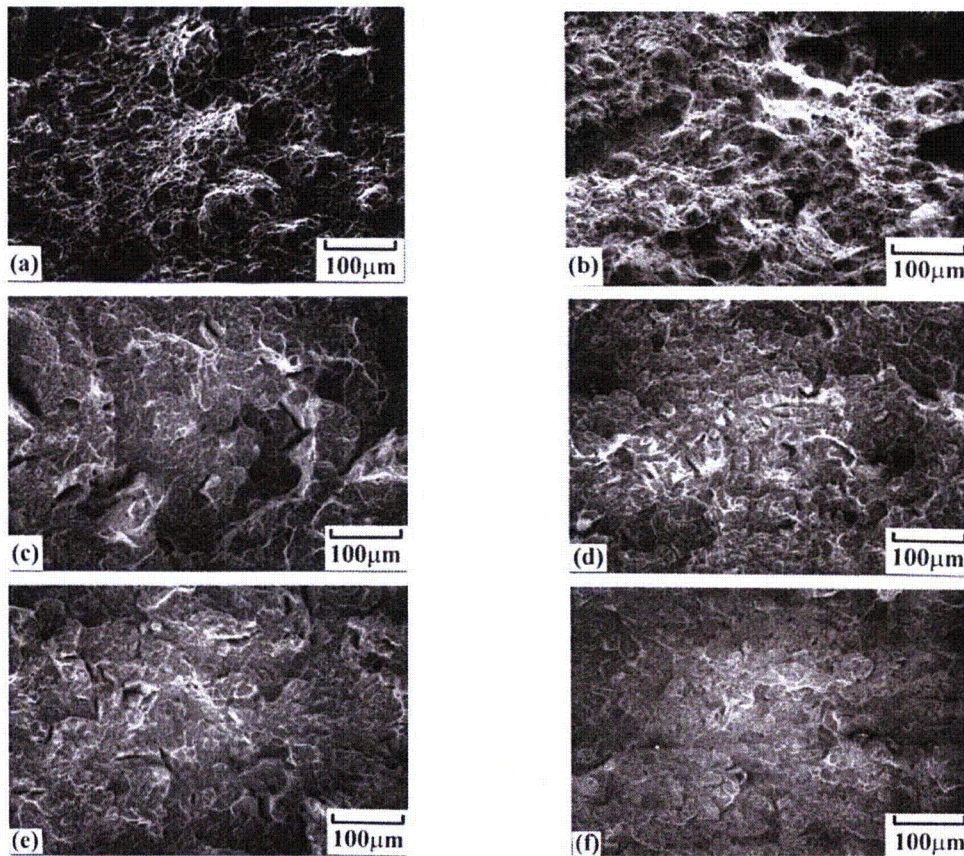


Fig. 5 Fractograph after impact testing of 2205 duplex stainless steel aged at 475°C for (a) 2h; (b) 4h; (c) 8h; (d) 16h; (e) 32h and (f) 64h

3.1.2 High temperature aging

The Charpy impact toughness results are presented in Fig. 6; it can be seen that the toughness decreases with the time of heat treatment. In the case of aging at 900 and 875°C, a drastic drop in toughness occurs after the aging time of only 5min. However, the decrease in toughness in the initial stage is much slower in the case of aging at 650°C. The severe deterioration in toughness for the steel aged at higher temperatures is presumed to be due to the formation of σ phase, which is known for its particularly harmful effect on toughness.

Figure 7 shows the variation of hardness as a function of aging time at different aging temperatures; it indicates that hardness increases with aging time at all temperatures. An apparent feature in Fig. 8 is the immediate response to aging at 900 and 875°C when compared with all other temperatures. For aging at 900 and 875°C, the hardness increases slowly in the early stage up to 30min and then increases sharply. However, the increase in hardness lags behind the mechanical effect on the toughness (Fig. 6). It is worth noting at this point that hardness alone cannot exactly reflect the presence of small amounts of σ phase.

Figure 8 shows Charpy impact energy as a function of aging time at 650 ~ 950°C. Each square symbol gives the impact energy at that particular aging time and temperature. Ahn and Kang [11] studied a series of 2205 duplex stainless steels, and claimed that the steels containing 2 ~ 5 vol% σ phase in the microstructure had impact energy of 32J. The impact value of 32J was therefore, chosen in the present work to represent approximately the transition from ductile to brittle fracture. The nose of ductile/brittle boundary in Fig. 8 is approximately at 900°C for 3min. The fracture

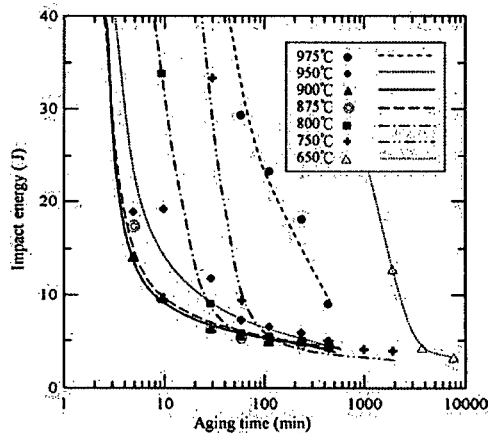


Fig. 6 Effect of aging treatments on Charpy V impact energy of 2205 duplex stainless steel aged at 650 ~ 975°C (Impact energy of as-received material: 304J)

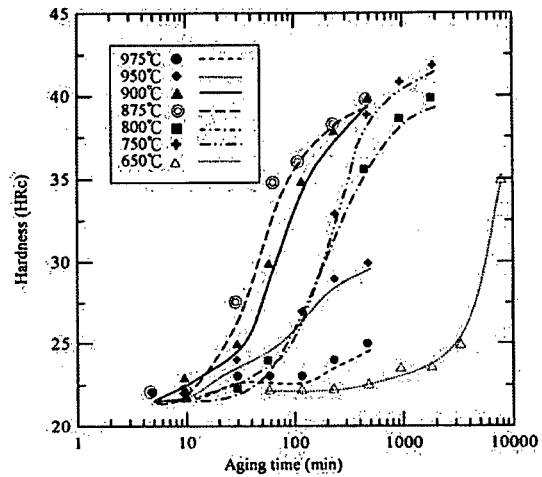


Fig. 7 Effect of aging treatments on HRC macro-hardness of 2205 duplex stainless steel aged at 650 ~ 975°C (Hardness of as-received material: HRC 22)

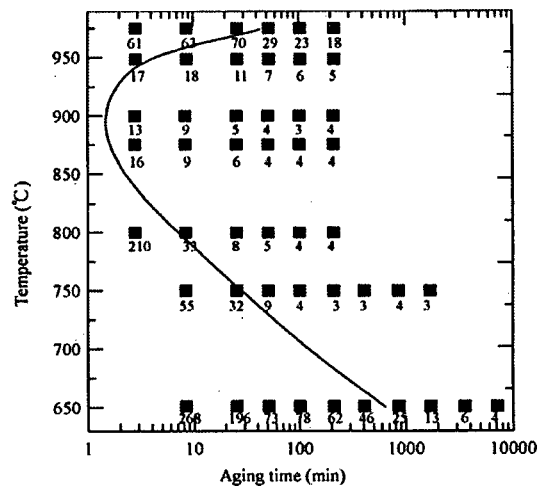


Fig. 8 Impact energy as function of aging temperature and time; solid line of 32J corresponding to 5 vol% σ phase precipitation

surface of the steel aged at 900°C for 5min (Fig. 9) provides an evidence to show that the quasi-cleavage areas were distributed uniformly over the entire fracture surface.

3.2 Microstructural Evolution During Aging

3.2.1 Low temperature aging

Field-emission gun transmission electron microscopy was used to investigate the detailed nano-scaled structure of the aged specimens. Figure 10 is an image taken from the δ/γ interface of the specimens

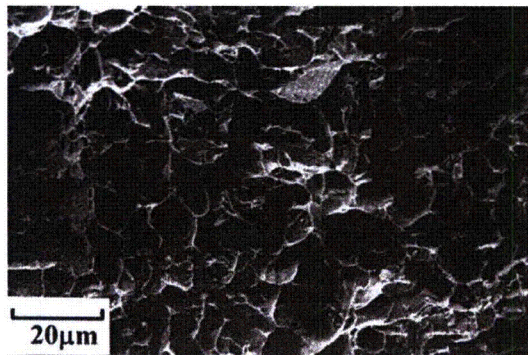


Fig. 9 Fractograph after impact testing of 2205 duplex stainless steel aged at 900°C for 5min

aged at 475°C for 2h. It is noticeable that there is a sudden change from the modulated contrast in δ -ferrite to an even contrast in γ . The mottled image of δ -ferrite can be seen much more clearly when the electron beam is aligned along the $\langle 001 \rangle$ zone axis. This result is consistent with that claimed by Nichol, *et al.* [12]. The mottled image, which has the appearance of an orange peel, has been found in TEM bright field micrographs of aged ferritic and duplex stainless steels. The mottled aspect has been attributed to the nucleation and growth of Cr-rich α' particles or to a spinodal decomposition reaction. The contrast mechanism is not clear, although it has been presumed to be due to differential oxidation of the two phases during the preparation of the TEM thin foils. Because of Fe and Cr partitioning at an extremely fine scale, the interpretation of the microstructural features should be made with care. However, earlier investigations using TEM failed to reveal the detailed nanometer-scaled structure and chemistry. On the other hand, atom probe field ion microscopy has revealed the phase separation due to the spinodal decomposition into an ultrafine mixture of a Cr-enriched α' and an Fe-rich α . Furthermore, the three-dimensional α' phase has been reconstructed by Miller, *et al.* [13,14], who suggests that the α' phase forms a typical complex interconnected network structure.

In the present investigation, a periodically modulated contrast (Fig. 10) occurs in the ferrite without a denuded zone in the immediate vicinity of the δ/γ interfaces. The evidence strongly suggests that the phenomenon of spinodal decomposition occurs in δ -ferrite during aging at 475°C. The morphology of the modulated microstructure for the specimens aged at 475°C is shown in Fig. 11. These micrographs reveal phase separation in the specimens aged for 2 ~ 64h, but it is difficult to resolve in specimens aged for less than 2h. The scale of this

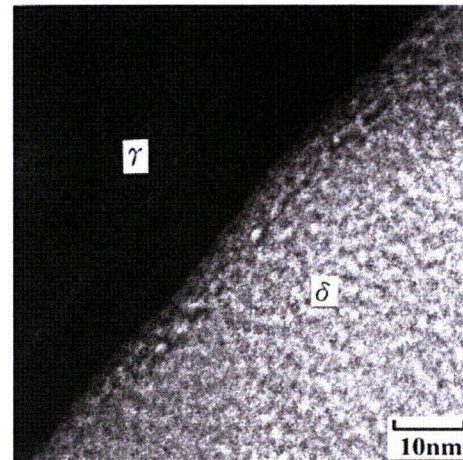


Fig. 10 FEG-TEM showing δ and adjacent γ in the specimen aged at 475°C for 2h

two-phase modulated microstructure has been measured to be 1.7, 2.5, 3.3, 4.2, 4.3 and 5.0nm for aging times of 2, 4, 8, 16, 32 and 64h, respectively. The modulated microstructure is observed to coarsen with aging time, the morphology being similar. The sequences of FEG-TEM (Fig. 11) reveal that the two-phase mixture is irregularly shaped and fully interconnected as resembling a sponge, indicative of the typical nature of the isotropic spinodal structure. Nanometer-scaled chemical analysis has been conducted using a FEG-TEM containing an EDS; the data for the specimen aged at 475°C for 64h is illustrated in Fig. 12. The fine scale isotropic spinodal decomposition of δ -ferrite brings about Cr-rich bright image domains and Fe-rich dark image domains; i.e., α' and α phases, separately. It also shows that Mo and Mn is partitioning to the α' phase, while Ni is partitioning to the α phase [15].

3.2.2 High temperature aging

The microstructural change during isothermal aging at 900°C is shown in Fig. 13. For the specimen aged at 900°C for 5min, tiny secondary particles were already found to precipitate at the ragged interfaces between γ island and δ -ferrite matrix. These interfaces have been well known as the preferential nucleation sites for the heterogeneous precipitation of σ phase [16]. The size and amount of σ phase increased with the aging time at 900°C, and σ phase eventually became the coarse particles with an irregular shape. Figures 13(c)(e) show the optical metallographs of the specimen aged at 900°C for 30 min to 2 h; they clearly reveal that σ phase formed along the γ/δ interfaces and grew into the

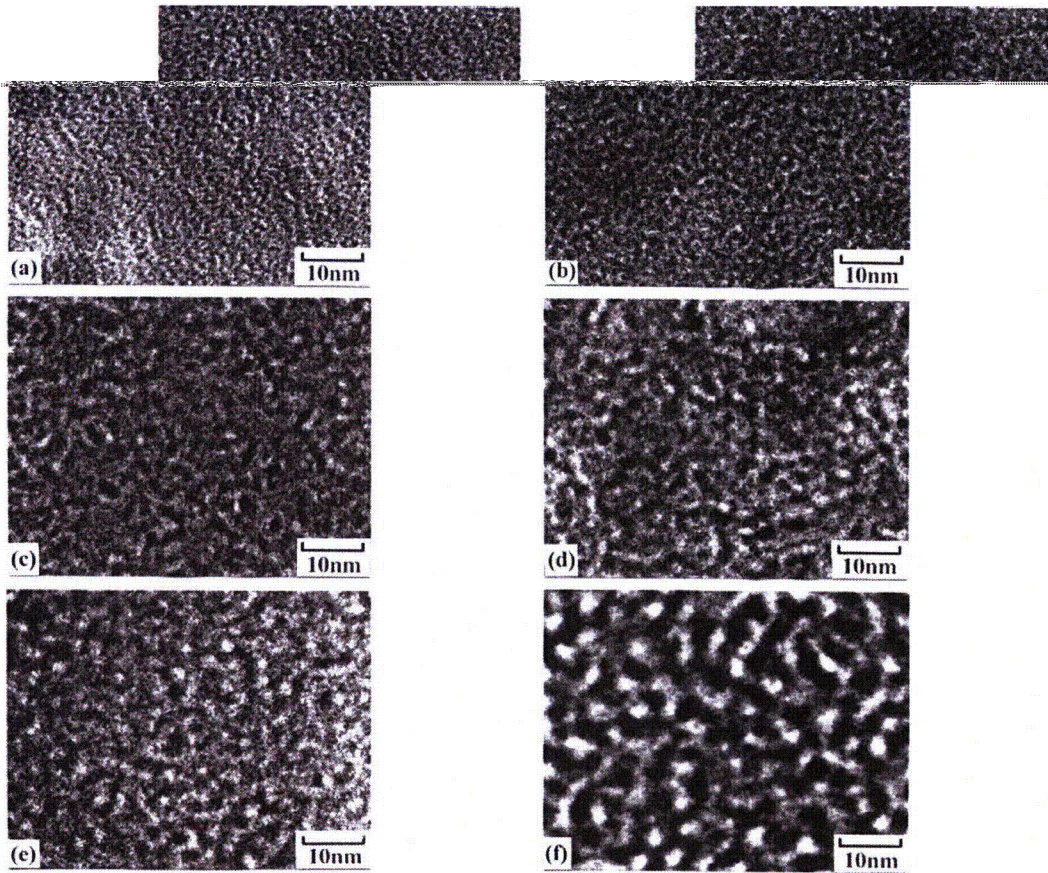


Fig. 11 FEG-TEM showing the morphology of the modulated microstructure for the specimens aged at 475°C for different time intervals: (a) 2h; (b) 4h; (c) 8h; (d) 16h; (e) 32h and (f) 64h

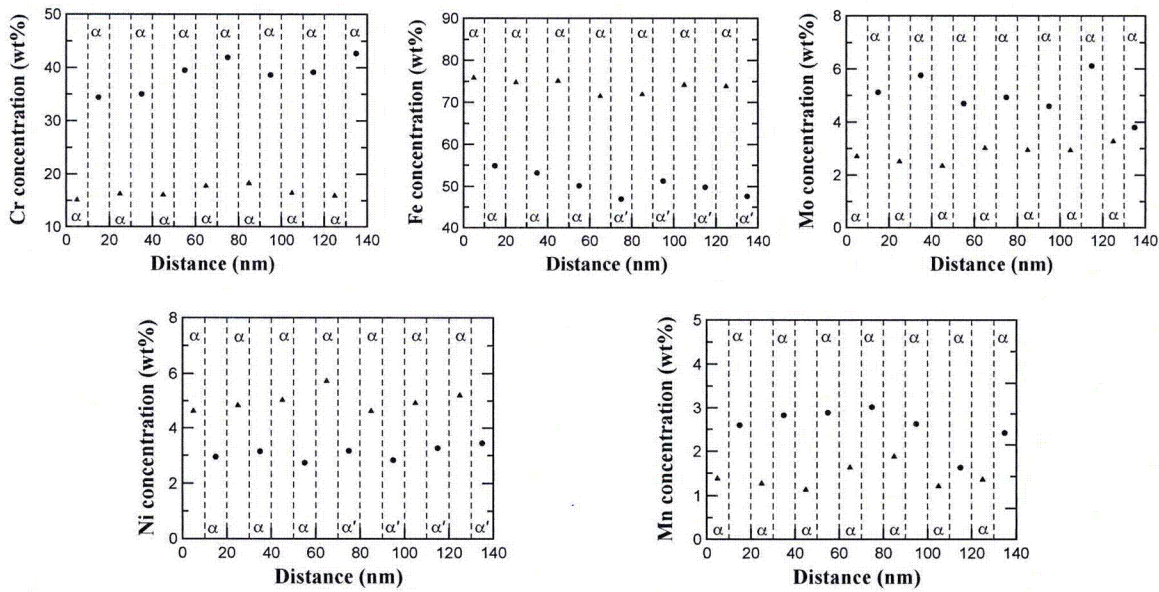


Fig. 12 The concentration profiles of α' and α phases obtained from the data of nano-scaled EDX analysis

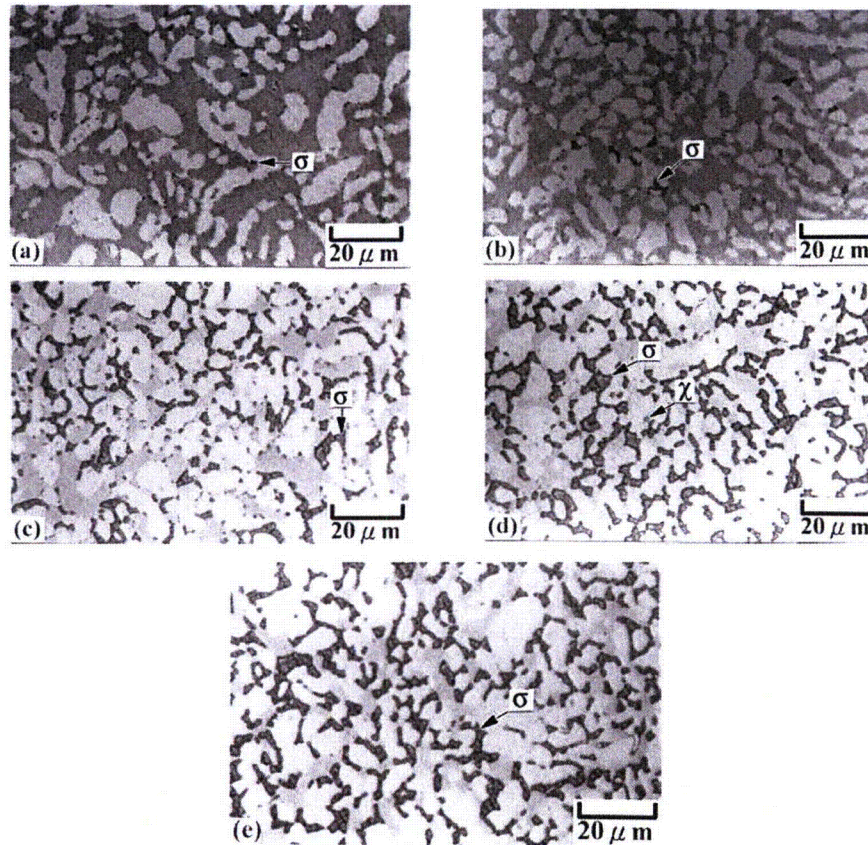


Fig. 13 Optical metallographs obtained from the specimens aged at 900°C for (a) 5min; (b) 10min; (c) 30min; (d) 1h and (e) 2h

adjacent δ -ferrite region. That the volume fraction of σ phase increases with the time of aging is responsible for the remarkable increase in hardness for the specimens aged at 900°C for longer holding times (Fig. 7).

The microstructural evolution during isothermal aging at 750°C is shown in Fig. 14. The amounts of secondary phases were much fewer at the initial stage of aging as compared with that formed in the specimens aged at 900°C for the same aging time (Fig. 13). No substantial precipitate could be detected under the observation of optical microscope until the aging time up to 10min. The small precipitates discretely precipitated at γ/δ interface in the aged specimen (Figs. 14(b) ~ 14(e)) were considered as the χ phase. The dark σ phase with a larger size than χ phase was locally precipitated and became the dominate precipitate as the aging time increased to 2h (Fig. 14(e)). The microstructures of specimens after the long-term aging at 650°C are shown in Fig. 15; the secondary precipitates began to precipitate at the boundaries of γ/δ and δ/δ until the aging time of 8h at 650°C (Fig. 15(a)). In

addition to the interfacial precipitates, they were small secondary particles, considered as the χ phase, discretely formed within the grain of δ -ferrite in the specimens aged for 16h and 32h (Figs. 15(b) and 15(c)). With the increase of aging time after 64h (Figs. 15(d) and 15(e)), large amounts of dark σ phase were spread toward the δ -ferrite region.

The serial optical metallographs for the aged specimens show that the amount of σ phase continuously increased with the time of aging, and that the χ phase, which once had precipitated at the initial stage of aging, grew restrictively with the prolonged aging. The result is in agreement with that reported by Karlsson, *et al.* [17], who investigated the transformation kinetics from χ phase to σ phase. As indicated on the phase diagram for a typical 2205 duplex stainless steel, the meta-stable δ -ferrite below 1000°C would be ultimately decomposed into Cr, Mo-enriched σ phase and Cr, Mo-depleted γ phase. In this work, the growth of σ phase was enhanced by the high diffusibility of solute atoms and consequently σ phase developed into a

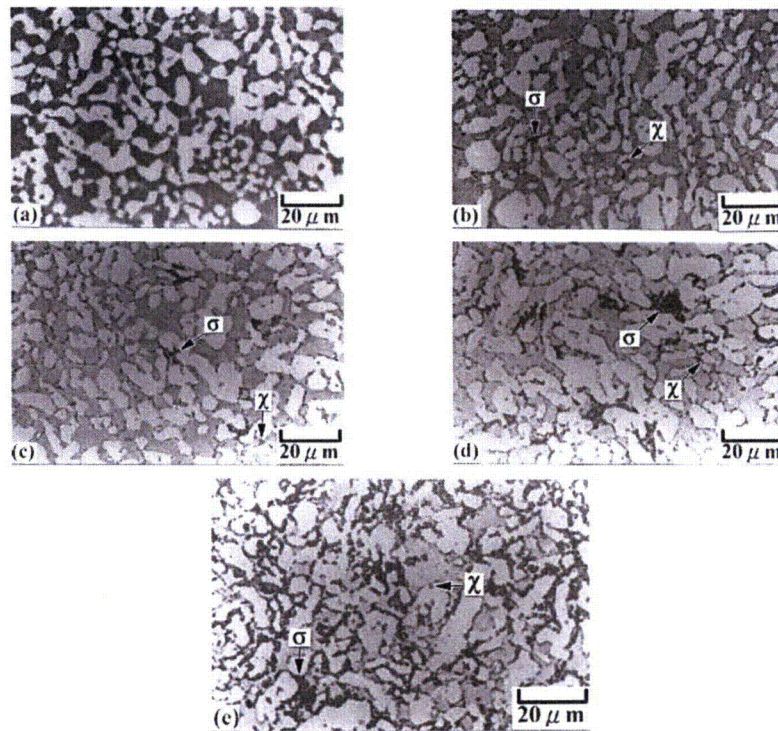


Fig. 14 Optical metallographs obtained from the specimens aged at 750°C for (a) 5min; (b) 10min; (c) 30min; (d) 1h and (e) 2h

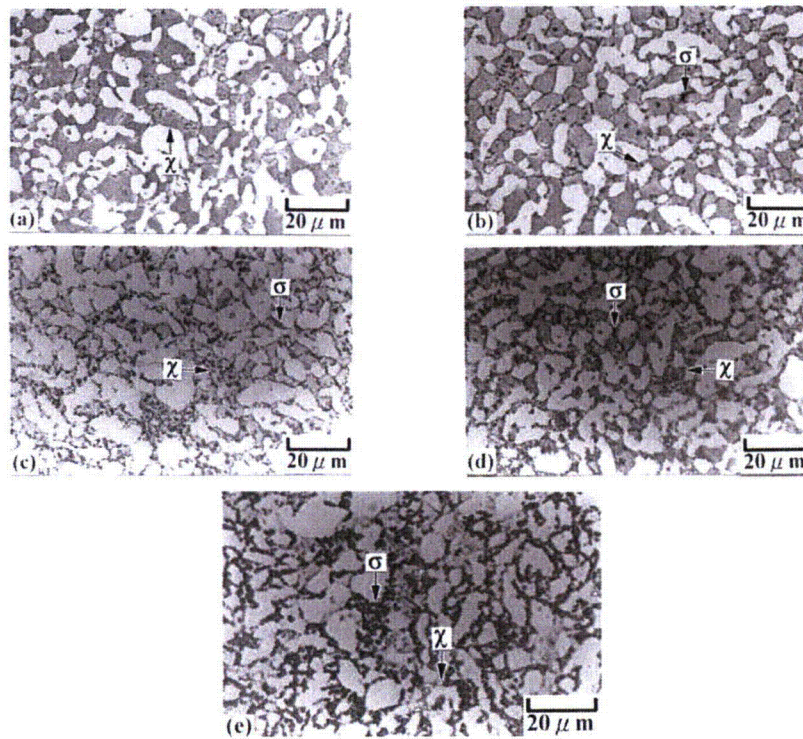


Fig. 15 Optical metallographs obtained from the specimens aged at 650°C for (a) 8h; (b) 16h; (c) 32h; (d) 64h and (e) 128h

coarse particle after the long-term aging. The chemical compositions of σ and χ phases were measured using the energy-dispersive X-ray (EDX) microanalysis as presented in Fig. 16. The EDX results revealed the dark-grey phase to be Cr-rich σ , and the light-grey phase to be Mo-rich χ .

3.3 TEM and HRTEM Observation

3.3.1 Low temperature aging

A series of microstructural features in the specimens aged at 475°C for different aging times has been studied by TEM. Figure 17 shows the morphologies of δ and γ obtained from the as-received sample (notice an annealing twin across the γ grain). TEM bright field images for the specimens aged at 475°C for different aging times have been observed under a two-beam condition as illustrated in Figs. 18 ~ 20. The striking feature from the above TEM micrographs indicates that the evolution of dislocation structure occurs in a form of cross-stitch in δ -ferrite during aging. The decomposed δ -ferrite with the complex dislocation structure is assumed to be due to the differences in thermal expansion between δ and γ phases, and it is also related to the cross-slip of dislocations during aging. A similar observation has been reported by Miller, *et al.*, [13], who investigated a duplex stainless steel, CF8, aged at 400°C for 7×10^4 h. The dislocation structure with a cross-stitch pattern is significant, since it provides strong support to suggest that the immobilization of dislocations in δ -ferrite is detrimental to toughness. However further work is needed in this area to understand the formation mechanism of these pinned dislocations in the aged δ -ferrite [100]. Electron diffraction patterns (Fig. 21(c)) taken from a selected area of the two-phase modulated structure shows only one set of b.c.c. diffraction spots without flanking satellites. It is apparent that the lattice mismatch between α' and α phases is extremely low ($a_{Cr} = 2.885\text{\AA}$, $a_{Fe} = 2.866\text{\AA}$ for the pure elements) although the α' phase has a high level of Cr. In the lattice image (Fig. 21(b)), it is difficult to identify the interfaces between the α' and α phases. Indeed, this lattice image reflects the nature of the isotropic spinodal structure; the elastic coherent strain of the interfaces is negligible and consequently the two-phase mixture is interconnected without directionality in the three dimensions. It should be noted that the result of the EDS analysis (Fig. 12) for the nanometer-scaled modulated structure can barely provide approximate compositions because of the complex three-dimensional percolated network morphology.

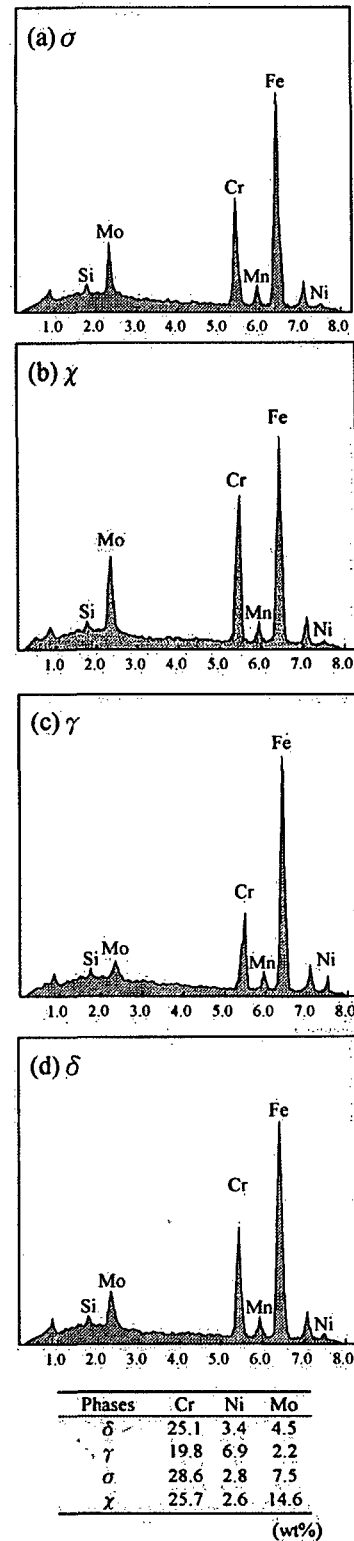


Fig. 16 Energy dispersive X-ray spectra and major alloy contents (a) σ ; (b) χ ; (c) γ and (d) δ -ferrite

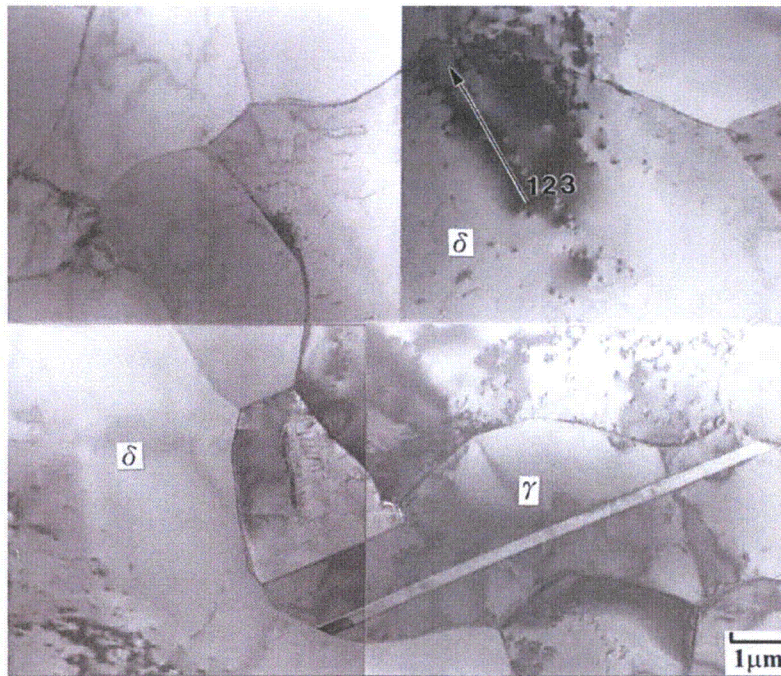


Fig. 17 The morphologies of δ and γ obtained from the specimen without aging; an annealing twin across the γ grain can be seen

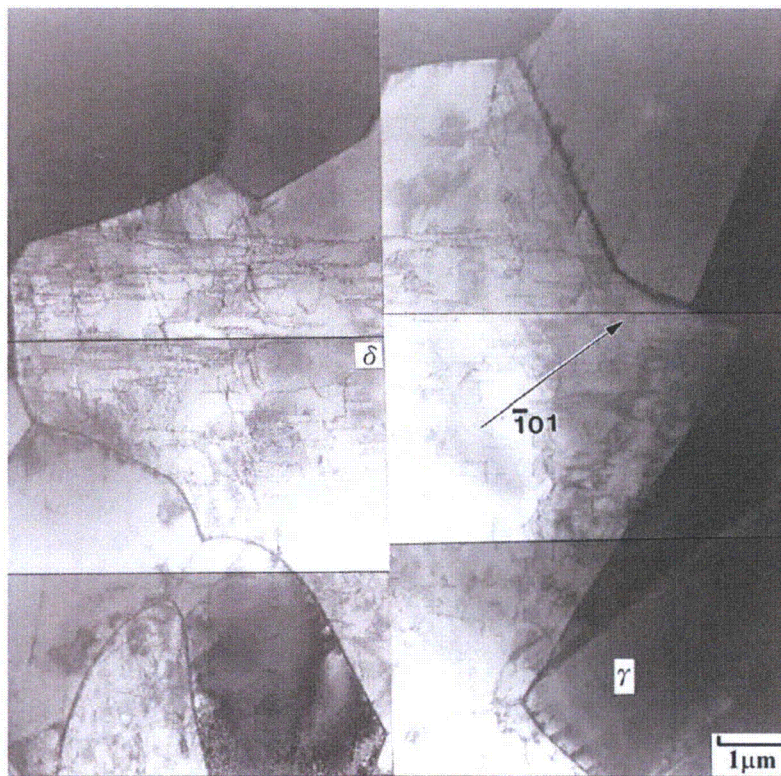


Fig. 18 Dislocation structure in δ -ferrite of the specimen aged at 475°C for 2h (Observation under two-beam condition $\bar{g} = [\bar{1}01]$)

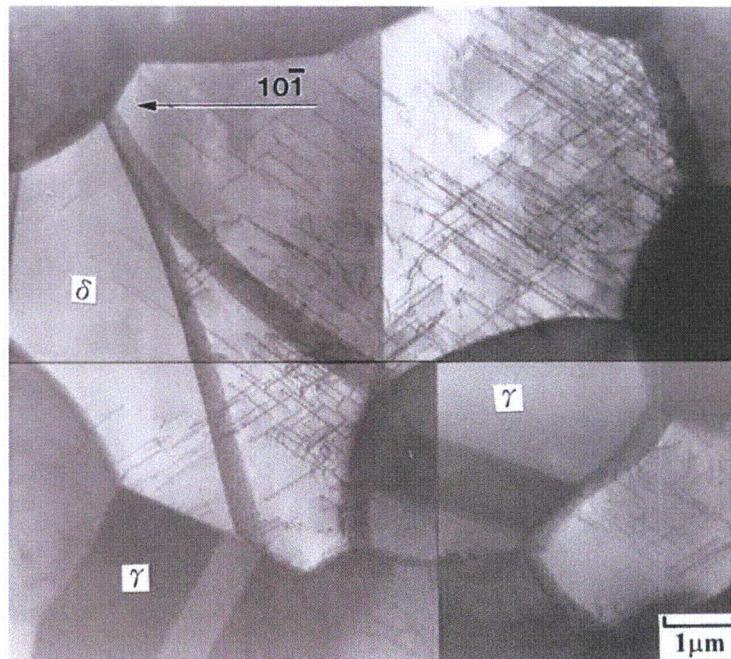


Fig. 19 Dislocation structure in δ -ferrite of the specimen aged at 475°C for 4h (Observation under two-beam condition $\bar{g} = [1\ 0\ \bar{1}]$)

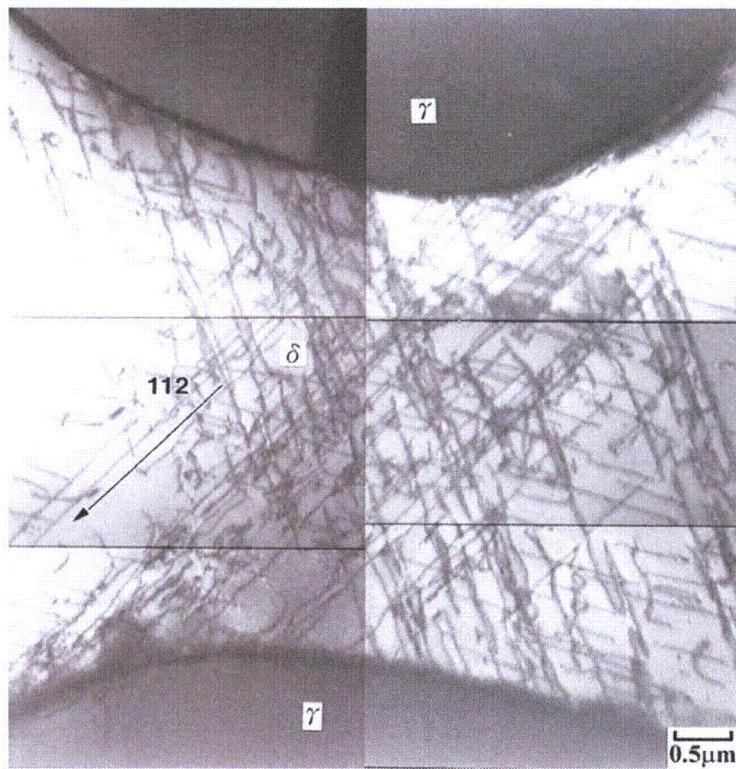


Fig. 20 Dislocation structure in δ -ferrite of the specimen aged at 475°C for 64h (Observation under two-beam condition $\bar{g} = [1\ 1\ 2]$)

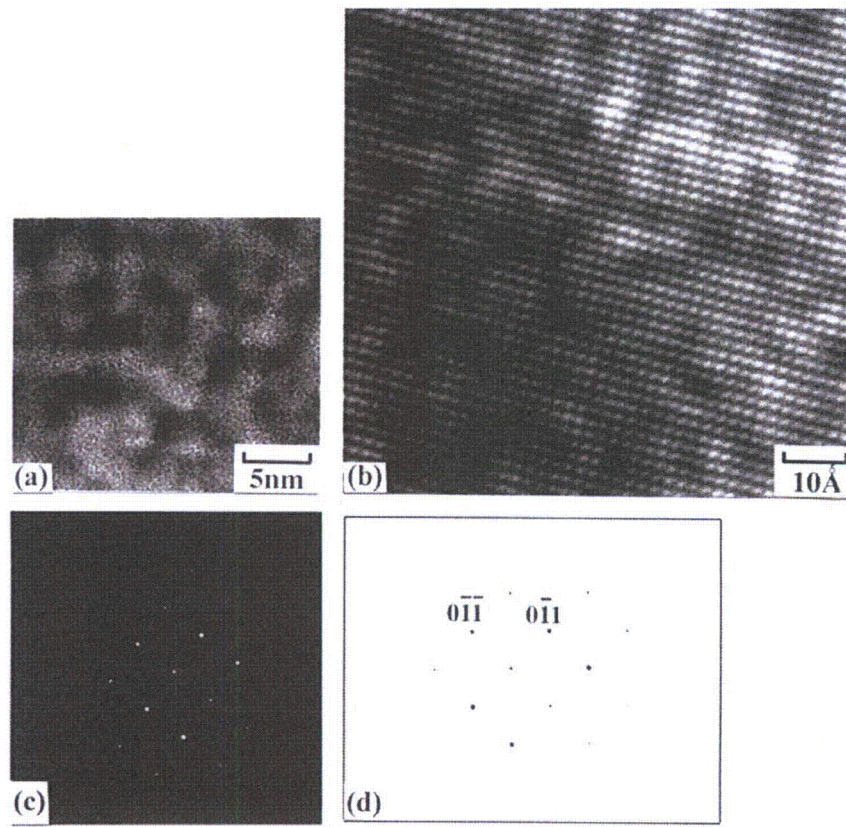


Fig. 21 High resolution images of a typical isotropic spinodal structure obtained from the specimen aged at 475°C for 64h: (a) modulated microstructure; (b) lattice image; (c) SAD diffraction pattern with [100] zone axis; (d) schematic interpretation of (c)

The dislocation mobility under a given condition of high-rate deformation may be inferred from the impact toughness. The two-phase interconnected structure corresponds to the marked drop of impact toughness and leads to the suggestion that the resistance to dislocation movement is proportional to the segregation of Cr and Fe in the developed spinodal structure. It should also be emphasized that the movement of dislocations by slip becomes more difficult in the Cr-rich domains since the friction stress is higher. This deformation mode is therefore expected shift from predominantly slip to prominently twinning. In this work, deformation twins within the decomposed δ -ferrite were commonly observed near the fracture surface of the impact test sample aged at 475°C for 64h as shown in Fig. 22.

3.3.2 High temperature aging

Figure 23 shows the transmission electron micrograph with the diffraction pattern of χ phase, which discretely precipitated at the prior γ/δ interface, in the specimen aged at 750°C for 10min. The boundary

of δ -ferrite nearby the χ precipitates was unstable due to the depletion of Cr, Mo at the local region. Consequently, the primary γ island grew progressively toward the region of δ -ferrite, and the χ particles were therefore enveloped within the newly formed γ .

An example for the co-precipitation of σ and χ phases is presented in the transmission electron micrograph of Fig. 24(a) for the specimen aged at 900°C for 10min. The χ particle was enveloped within the σ phase. The dissolving small χ particle (marked by an arrow in Fig. 24(b)) indicates that the meta-stable χ phase, which had formed at the initial stage of aging, transformed into σ phase after a prolonged aging. Figure 25 shows the extending σ phase grew toward the region of δ -ferrite along γ grain-boundaries after a long-term aging at 900°C for 1h. The growth manners of σ phase could be attributed to the partitioning of Cr and Mo in δ -ferrite and the close-packed structure of γ phase.

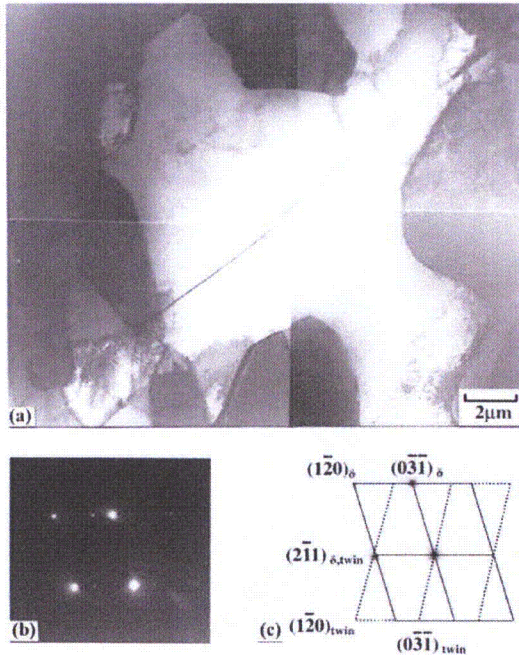


Fig. 22 TEM showing the deformation twins within the decomposed δ -ferrite observed near the fracture surface of the impact test sample aged at 475°C for 64h: (a) bright field image; (b) diffraction pattern with zone $[\bar{2} \bar{1} 3]$; (c) interpretation of the diffraction pattern (b)

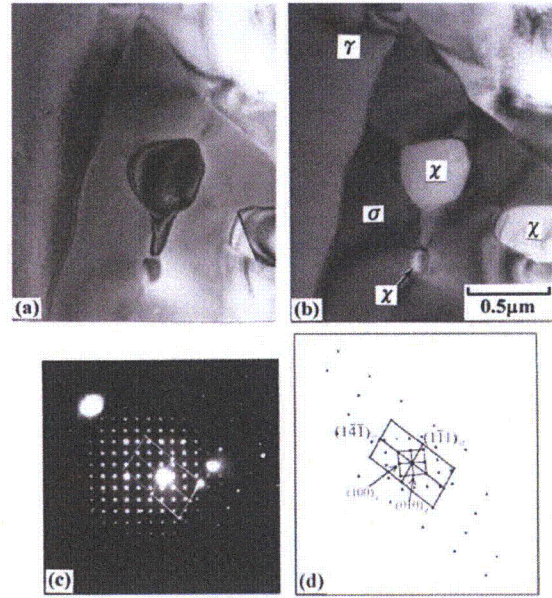


Fig. 24 Microstructure of the specimen aged at 900°C for 10min: (a) bright field image; (b) corresponding dark field image of TEM micrograph showing χ particles within σ precipitate; (c) selected area diffraction pattern with zone axes of $[5 \ 2 \ \bar{3}]_{\sigma} // [001]_{\chi}$; (d) interpretation of (c)

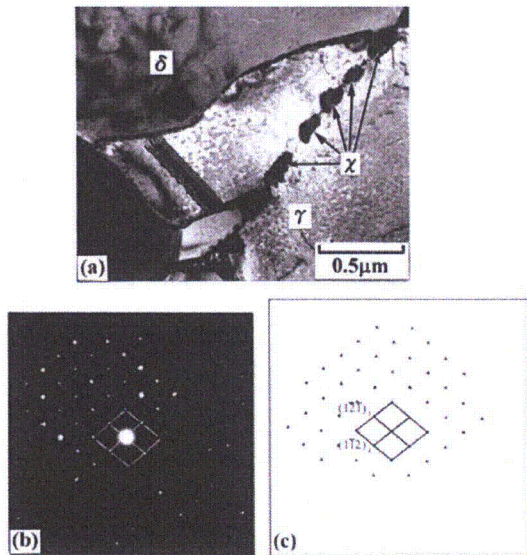


Fig. 23 Microstructure of the specimen aged at 750°C for 10min: (a) Transmission electron micrograph showing small χ particles precipitated discretely at the prior δ/γ interface; (b) diffraction pattern with zone $[\bar{5} \ \bar{3} \ 1]_{\chi}$; (c) interpretation of (b)

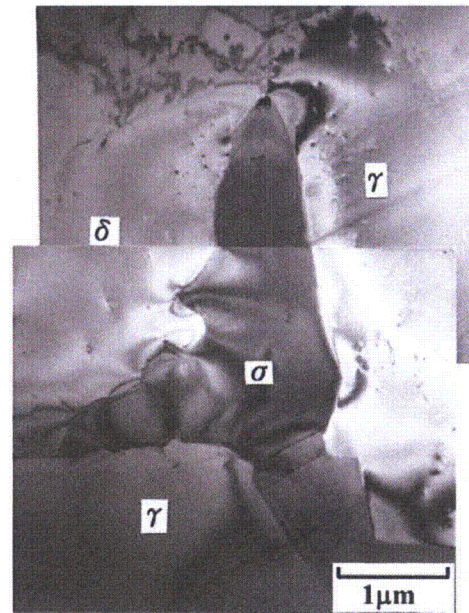


Fig. 25 Transmission electron micrograph obtained from the specimen aged at 900°C for 1h showing coarse σ precipitate grown toward δ -ferrite region

4. CONCLUSIONS

An aging embrittlement at temperatures ranging between 400 and 975°C and a corresponding phase transformation in a 2205 duplex stainless steel have been investigated. A summary of the experimental outcome is given as follows:

1. The evidence shows that the intermetallic σ phase precipitated at the interface of γ/δ in the specimen within 5 min of aging at 900°C. That the σ phase grew into the coarse particles is presumed due to the high diffusivity of solute atoms at the high temperature. However, the eutectoid transformation from δ -ferrite to σ and γ phases was observed in the specimen aged at 750°C.
2. The impact toughness of duplex stainless steel was sensitive to the precipitation of σ phase even at the beginning of aging. For aging at 900 and 875°C, a drastic drop in toughness occurs after the aging time of only 5min. However, the hardness increases slowly in the early stage up to 30min and then increases sharply. The time taken for the increase in hardness substantially lags behind that taken for the drop in toughness.
3. The region of γ phase nearby the Cr, Mo-enriched secondary precipitates (σ or χ phases) was induced to grow toward the δ -ferrite region during the prolonged aging. Consequently, the secondary precipitates were enveloped within the newly formed γ . The evidence from transmission electron microscopy also suggests that χ phase is much more unstable than σ phase and would eventually transform to σ phase.
4. The results of fractography indicate that the phenomenon of embrittlement occurs significantly at 475°C; δ -ferrite exhibits an increasing tendency to quasi-cleavage failure with increasing aging times, and the fracture mode of austenite shifts from normal dimple rupture towards the tearing rupture.
5. The aging embrittlement at 475°C corresponds to the development of a two-phase modulated microstructure of δ -ferrite; the modulated structure coarsens with aging time, but the morphology is similar. FEG-TEM reveals that this two-phase mixture is irregularly shaped and fully interconnected as spongelike, indicative of a typical isotropic spinodal structure.
6. Dislocation structures with a cross-stitch pattern in the aged δ -ferrite provides strong evidence to suggest

that the immobilization of dislocations in this modulated structure causes severe embrittlement.

7. The contrast mechanism for this modulated structure is not clear, and it needs further investigation to elucidate the factors which govern the mottled aspect in the present work.

ACKNOWLEDGEMENTS

This work was carried out with financial support from the National Science Council of Republic of China, under Contract NSC 91-2216-E-002-026. The authors thank Gloria Material Technology Corporation for providing the steel rods.

REFERENCES

- [1] J. Charles, "Materials to meet your needs," *Proceedings of International Conference on Duplex Stainless Steels*, Editors: J. Charles and Bernhardsson, Vol. 1, Beaune Bourgogne, France, October 1991, pp. 3–48.
- [2] M. E. Wilms, V. J. Gadgil, J. M. Krougman and B. H. Kolster, "The effect of σ -phase precipitation at 800°C on the mechanical properties of a high alloyed duplex stainless steel," *Materials at High Temperature*, Vol. 9, No. 3, August 1991, pp. 160–166.
- [3] S. B. Kim, K. W. Paik and Y. G. Kim, "Effect of Mo substitution by W on high temperature embrittlement characteristics in duplex stainless steels," *Mater. Sci. Eng.*, Vol. A247, 1998, pp. 67–74.
- [4] O. A. Hilders, L. Saenz, M. Ramos and N. D. Pena, "Effect of 475°C embrittlement on fractal behavior and tensile properties of a duplex stainless steel," *Journal of Materials Engineering and Performance*, Vol. 8, No. 1, February 1999, pp. 87–90.
- [5] M. K. Miller, J. M. Hyde, A. Cerezo and G. D. W. Smith, "Comparison of low temperature decomposition in Fe-Cr and duplex stainless steels," *Applied Surface Science*, Vol. 87/88, 1995, pp. 323–328.
- [6] H. M. Chung and T. R. Leax, "Embrittlement of laboratory and reactor aged CF3, CF8, and CF8M duplex stainless steels," *Materials Science and Technology*, Vol. 6, March 1990, pp. 249–262.
- [7] P. H. Pumphrey and K. N. Akhurst, "Aging kinetics

- of CF3 cast stainless steel in temperature range 300 ~ 400°C," *Materials Science and Technology*, Vol. 6, March 1990, pp. 211-219.
- [8] T. R. Leax, S. S. Brenner and J. A. Spitznagel, "Atom probe examination of thermally aged CF8M cast stainless steel," *Metallurgical Transactions A*, Vol. 23A, 1992, pp. 2725-2736.
- [9] P. Auger, F. Danoix, A. Menand, S. Bonnet, J. Bourgoïn and M. Guttman, "Atom probe and transmission electron microscopy study of aging of cast duplex stainless steels," *Materials Science and Technology*, Vol. 6, March 1990, pp. 301-313.
- [10] S. Bonnet, J. Bourgoïn, J. Champredonde, D. Guttman and M. Guttman, "Relationship between evolution of mechanical properties of various cast duplex stainless steels and metallurgical and aging parameters: outline of current EDF programmes," *Materials Science and Technology*, Vol. 6, March 1990, pp. 221-229.
- [11] Y. S. Ahn and J. P. Kang, "Effect of aging treatments on microstructure and impact properties of tungsten substituted 2205 duplex stainless steel," *Materials Science and Technology*, Vol. 16, April 2000, pp. 382-387.
- [12] T. J. Nichol, A. Datta and G. Aggen, "Embrittlement of ferritic stainless steel," *Metallurgical Transactions A*, Vol. 11A, April 1980, pp. 573-585.
- [13] M. K. Miller and J. Bentley, "APFIM and AEM investigation of CF8 and CF8M primary coolant pipe steels," *Materials Science and Technology*, Vol. 6, March 1990, pp. 285-292.
- [14] M. K. Miller and M. G. Hetherington, "Morphology and scaling behavior of ultrafine isotropic microstructures in Fe-Cr alloys from atom probe field ion microscopy data," *Scripta Metallurgica*, Vol. 24, 1990, pp. 1375-1380.
- [15] H. D. Solomon and L. M. Levinson, "Mössbauer effect study of '475°C embrittlement' of duplex and ferritic stainless steels," *Acta Metallurgica*, Vol. 26, 1978, pp. 429-442.
- [16] B. Josefsson, J. O. Nilsson and A. Wilson, "Materials to meet your needs," *Proceedings of International Conference on Duplex Stainless Steels*, Editors: J. Charles and Bernhardsson, Vol. 1, Beaune Bourgogne, France, October 1991, pp. 67-78.
- [17] L. Karlsson, L. Bengtsson, U. Rolander and S. Pak, *Proceedings of International Conference on Applications Stainless Steel*, The Institute of Metals, Stockholm, Sweden, 1992, pp. 335-344.



Kuang Liang Weng (翁光良) 民國 54 年生，目前就讀台灣大學材料科學與工程學研究所博士班。民國 87 年畢業於大同大學材料工程學研究所碩士班。研究領域：顯微結構分析，鋼鐵相變態。



Tung Hung Chen (陳東宏) 民國 56 年生，目前任職於聯電公司。民國 91 年畢業於台灣大學材料科學與工程學研究所博士班。



Jer Ren Yang (楊哲人) 國立台灣大學材料科學與工程學研究所教授，民國 43 年生，民國 67 年畢業於成功大學冶金及材料工程學系，民國 69 年畢業於清華大學材料科學工程研究所碩士班，民國 76 獲得英國劍橋大學材料科學博士學位。研究領域：顯微結構分析、金屬相變態、材料缺陷。

收稿日期 92 年 7 月 1 日、修訂日期 92 年 9 月 25 日、接受日期 92 年 10 月 4 日
Manuscript received July 1, 2003, revised September 25, 2003, accepted October 4, 2003

Summary of Changes, TRUPACT-III SAR DRAWING – 51199-SAR, Rev. 1			
Sheet	Zone	Change Description	Justification
1	A-1/2	Revised the company name from "PACKAGING TECHNOLOGY INC" to "AREVA FEDERAL SERVICES LLC"	Administrative change. No impact to safety basis.
1	B-1	I/Ns 6 & 7: Added Type 304 as an option to Type 304L.	Change allows the use of a material having same mechanical properties. No impact to safety basis.
1	C-1	I/N 19: Added ASTM A479 bar stock as an option to ASTM A240 plate stock.	Change allows the use of bar material as an option to plate material. No impact to safety basis.
1	C-1	I/N 29: Revised the material for vent port insert.	Reflect material that was used in certification tests. No impact to safety basis.
1	A-5	I/N 44, 45, & 47: Added Type 304 material as an option to Type 304L material.	Change allows the use of a material having same mechanical properties. No impact to safety basis.
1	A-7	I/N 46: Increased material thickness from 30 mm to 50 mm	Revised material thickness for the debris shield holder as a continuous part in lieu of a weldment. No impact to safety basis.
1	A-8	I/N 47: Increased quantity of bars from 8 to 11.	Added quantity to reflect the added SBL2 guide bars on the rear end of the cavity. No impact to safety basis.
1	A-5/8	I/N 53: Revised the size, quantity, and material for the plastic plates that now attach to the rear SLB2 guide bars.	Changes reflect the current configuration for minimizing gap between SLB2 and closure lid. Improved safety basis.
1	B-5	I/Ns 54, 58, & 59: Added UNS S31803 as optional material for guide pins on closure lid and overpack cover, closure lid lifting blocks, and overpack cover guide pin receptacle.	Optional material allowed for operational considerations. No impact to safety basis.
1	B-5	I/N 65: Added Type 304L as an optional material for debris shield receptacle.	Added material that was used in certification tests. No impact to safety basis.
1	A-5/8	I/N 66: Revised material, quantity and specification, and flag note for attaching the rear plastic SLB2 guide bar plates.	Changes reflect the current configuration for minimizing gap between SLB2 and closure lid. Improved safety basis.

Summary of Changes, TRUPACT-III SAR DRAWING – 51199-SAR, Rev. 1			
Sheet	Zone	Change Description	Justification
1	A-5/7	I/N 68: Added manufacturer and part number for polyethylene passive vents.	Added information provides more specificity to ensure item matches parts used in certification tests. No impact to safety basis.
1	C-7	General Note 5: Corrected weight of contents.	Change reflects current payload configuration. No impact to safety basis.
1	C-6/7	Flag Note 14: Added "USING A FLARE BEVEL WELD".	Change clarifies weld joint for optional configuration of thin sheets on overpack cover. No impact to safety basis.
1	D-5/6	Flag Note 21: Added manufacturer and part number for containment O-ring seals.	Added information provides more specificity to ensure seals match those used in certification tests. No impact to safety basis.
2	D-8	Flag Note 32: Revised note for the now required integral debris shield holder by changing to THE LID.	Administrative change. No impact to safety basis.
2	C-6/8	Flag Note 35: Revised note to replace the previous rubber strips to the current configuration of using a plastic plate machined to adjust the cavity length.	Change reflects the current configuration for minimizing gap between SLB2 and closure lid. Improved safety basis.
2	C-7	Flag Note 39: Added "CLASS 2" to cadmium plating specification.	Added missing information to ensure correct plating is utilized for SHCSs. No impact to safety basis.
2	C-6/8	Flag Note 42: Revised to add test port option to all components that may weld to containment boundary. Original note text no longer applicable.	Option necessary to eliminate potential virtual leak paths during leakage rate tests of metallic containment boundary. No impact to safety basis.
2	C-6/8	Flag Note 44: Added to add optional thread locking compound for flat head machine screws used to secure the plastic plates to the rear SLB2 guide bars.	Option added for operational considerations. No impact to safety basis.
2	C-6/8	Flag Note 45: Added to add seal weld requirement for debris shield receptacle weld joints.	Requirement necessary to located and eliminate virtual leak paths if any are found during leakage rate tests of metallic containment boundary. No impact to safety basis.

Summary of Changes, TRUPACT-III SAR DRAWING – 51199-SAR, Rev. 1			
Sheet	Zone	Change Description	Justification
2	C-6/8	Flag Note 46: Added to clarify weld size following machining operations.	Weld is made prior to machining of body flange; minimum weld size is required to ensure final weld matches configuration used in certification tests. No impact to safety basis.
4	A-3 B-3	Section D-D: Clarified view by adding "ROTATED 90° CCW". Revised view of bolt bar	Administrative change. No impact to safety basis.
4	A-5	Detail Item 3: Added detail for flat washers utilized with the SHCSs to secure the closure lid and overpack cover.	Added missing detail from initial application. No impact to safety basis.
4	A-7 B-7	Revised view of bolt bar in enlarged details (2 places).	Administrative change. No impact to safety basis.
4	C-4/5	Updated enlarged view of debris shield holder and passive filter.	Change reflects current configuration. No impact to safety basis.
4	C-6/7	Section B-B: Added "2752 ±3, (EFFECTIVE INTERNAL CAVITY LENGTH)" to reflect current configuration.	Change reflects the current configuration for minimizing gap between SLB2 and closure lid. Improved safety basis.
4	D-3	Detail E: Revised view of bolt bar.	Administrative change. No impact to safety basis.
4	D-5	Added "STAKE IN PLACE" for passive filters in enlarged view.	Method of installation provides more specificity to ensure installation matches what was used in certification tests. No impact to safety basis.
4	D-6	Section B-B: Added "TO WALL" to internal cavity length dimension.	Clarification was required to reflect current configuration. No impact to safety basis.
5	A-5/7 B-6	Added Section BS-BS for attaching rear plastic bars to rear SLB2 guide bars.	New section required to reflect current configuration. No impact to safety basis.
5	B-2	Revised thickness of polyurethane foam part from "174" to "176".	Corrected thickness to actual thickness of polyurethane foam part. No impact to safety basis.

Summary of Changes, TRUPACT-III SAR DRAWING – 51199-SAR, Rev. 1			
Sheet	Zone	Change Description	Justification
5	B-6/8 C-6/8	Updated BODY ASSEMBLY A2 to reflect current configuration.	Change reflects the current configuration for minimizing gap between SLB2 and closure lid. No impact to safety basis.
5	Various	Section F–F: Updated section to reflect current configuration of rear SLB2 guide bars/plastic plate, and updated view of bolt bars for closure lid bolts.	Change reflects the current configuration for minimizing gap between SLB2 and closure lid. Improved safety basis.
6	C-1/2	Section G–G: Deleted duplicate weld callout.	Administrative change. No impact to safety basis.
6	C-3 C-5	Section G–G: Updated section to reflect current configuration of rear SLB2 guide bars/plastic plate, and updated view of bolt bars for closure lid bolts.	Change reflects the current configuration for minimizing gap between SLB2 and closure lid. No impact to safety basis.
6	D-8	Deleted dimension for pop rivet location.	Pop rivet is not a structural member for puncture resistant plate; rivet holds plate for assembly only. No impact to safety basis.
7	C-2	Revised weld callout for skewed fillet weld from “8” to “5”.	Previous weld callout incorrectly specified weld size for a skewed fillet weld. No impact to safety basis.
7	Various	Section H–H: Updated to reflect current configuration of rear SLB2 guide bars/plastic plate, including height dimensions to position correctly w/r to SLB2.	Change reflects the current configuration for minimizing gap between SLB2 and closure lid. No impact to safety basis.
9	A-2	Added “(SHT 5)” to Partial Section AS–AS.	Administrative change. No impact to safety basis.
9	A-3/4	Updated Partial Section AS–AS to reflect current configuration.	Change reflects the current configuration for minimizing gap between SLB2 and closure lid. No impact to safety basis.
10	A-1 B-2	Revised callout for ISO corner in View BR–BR.	Administrative change. No impact to safety basis.
10	B-1	Added missing liquid penetrant examination for weld joint in View BR–BR.	Nondestructive examination specification for weld was missing from initial application. No impact to safety basis.

Summary of Changes, TRUPACT-III SAR DRAWING – 51199-SAR, Rev. 1			
Sheet	Zone	Change Description	Justification
10	Various	Updated BODY ASSEMBLY, PARTIAL ISOMETRIC, FRONT VIEW to reflect current configuration. Change added missing Joloda rails in the floor, corrected ISO corner callout, and clarified weld callout for beveled joint for "picture frame" plates.	Administrative change. No impact to safety basis.
11	A-5	Revised callout for ISO corner.	Administrative change. No impact to safety basis.
11	B-7	Corrected from I/N 24 to I/N 13 for rear end outer plate.	Administrative change. No impact to safety basis.
12	B-2/3	Added drain hole to upper ISO corners.	Drain hole necessary to prevent collection of water in upper ISO corners. No impact to safety basis.
12	C-3 D-2/4	Added specific tolerances to ISO corner dimensions to ensure proper fit-up to ISO lifting lug.	Administrative change. No impact to safety basis.
13	A-6/8	Sections AB-AB and AC-AC: Updated to reflect current configuration for debris shield holder.	Update reflects elimination of welded configuration as an option to integral configuration. No impact to safety basis.
13	C-1	Section S-S: Updated to reflect current configuration for debris shield holder.	Update reflects elimination of welded configuration as an option to integral configuration. No impact to safety basis.
13	C-3	Section T-T: Updated enlarged detail to reflect current configuration for debris shield holder.	Update reflects elimination of welded configuration as an option to integral configuration. No impact to safety basis.
14	A-1/3	Added View BT-BT to reflect current configuration for debris shield holder.	View added to clarify debris shield holder configuration. No impact to safety basis.
14	A-3/4	Section W-W: Updated enlarged detail to reflect current configuration for debris shield holder.	Update reflects elimination of welded configuration as an option to integral configuration. No impact to safety basis.
14	A-6	Section W-W: Updated to reflect current configuration for debris shield holder.	Update reflects elimination of welded configuration as an option to integral configuration. No impact to safety basis.

Summary of Changes, TRUPACT-III SAR DRAWING – 51199-SAR, Rev. 1			
Sheet	Zone	Change Description	Justification
14	B-3 C-3 D-3	Detail Y: Updated to reflect current configuration for debris shield holder.	Update reflects elimination of welded configuration as an option to integral configuration. No impact to safety basis.
14	C-4	Detail Y: Corrected bevel weld orientation for attaching I/N 52 to I/N 46.	Change reflects actual weld joint that was used in certification test units. No impact to safety basis.
14	D-3	Detail Y: Revised surface specification from 3.2 micro-millimeters to 0.8 micro-millimeters	Change reflects correct surface finish that was used in certification test units. No impact to safety basis.
14	C-5	Detail Y: Changed liquid penetrant examination for weld joint from ASME NF to ASME NB.	Change reflects actual inspection criteria utilized for certification test units. No impact to safety basis.
14	C-5/6/7 D-5/6/7	CLOSURE LID ASSEMBLY: Updated to reflect current configuration, and added View BT-BT callout.	Change reflects the current configuration for minimizing gap between SLB2 and closure lid. No impact to safety basis.
15	B-5	Detail X: Revised liquid penetrant examination for weld joint from ASME NF to ASME NB.	Change reflects actual inspection criteria utilized for certification test units. No impact to safety basis.
15	C-1/2 D-2	Section AA-AA: Updated to reflect current configuration for debris shield holder.	Update reflects elimination of welded configuration as an option to integral configuration. No impact to safety basis.
16	A-7/8	Section AG-AG: Simplified fillet weld callouts for overpack cover lift components in.	Administrative change. No impact to safety basis.
16	B-4/5	Section P-P: Clarified view by adding "ROTATED 45° CW".	Administrative change. No impact to safety basis.
16	C-2	OVERPACK COVER ASSEMBLY: Revised tolerances for distance between overpack cover lips from "2300 +0/-8" to "2300 ±4".	Change added tighter tolerances to reduce the potential movement of cover relative to closure lid. Improved safety basis.
16	D-5	Corrected enlarged detail of weld joint in enlarged detail.	Administrative change. No impact to safety basis.
16	D-6/7	Corrected groove weld callout for the actual joint.	Administrative change. No impact to safety basis.

Summary of Changes, TRUPACT-III SAR DRAWING – 51199-SAR, Rev. 1			
Sheet	Zone	Change Description	Justification
16	D-7	OVERPACK COVER ASSEMBLY: Revised tolerances for overpack cover width from "2108 +0/-8" to "2108 ±4".	Change added tighter tolerances to reduce the potential movement of cover relative to closure lid. Improved safety basis.
17	A-5	Revised tube protrusion from "5" to "6" in enlarged detail.	Change was necessary to ensure sufficient tube length exists for affixing tamper indicating seals. No impact to safety basis.
17	D-2	Deleted pop rivet location dimension in enlarged detail.	Pop rivet is not a structural member for puncture resistant plate; rivet holds plate for assembly only. No impact to safety basis.
17	D-3	Section AE-AE: Revised length of overpack cover lips from "270" to "272", and "334" to "336".	Change reflects actual length of part used in certification test units. No impact to safety basis.
17	D-5	Corrected view of tube edge in enlarged detail.	Administrative change. No impact to safety basis.
18	B-2/3	Section AM-AM: Added seal weld callout for inside joints, and correct configuration of parts.	Change reflects actual configuration of certification test units. No impact to safety basis.
19	A-3	Deleted doubled dimension error for debris shield receptacle in enlarged detail.	Debris shield receptacle centerline dimension is controlled by the specified dimensions for the CSA opening, and the fit-up with the 20-mm wide step on the closure lid. No impact to safety basis.
19	A-6	Revised liquid penetrant examination for weld joint from ASME NF to ASME NB, and added new flag note 45 for debris shield receptacle in enlarged detail.	Change reflects actual inspection criteria utilized for certification test units. New flag note eliminates potential virtual leak paths during leakage rate tests of metallic containment boundary. No impact to safety basis.
19	B-1/2 B-4 C-2 D-4	Section BC-BC: Updated to reflect current configuration of rear SLB2 guide bars, and closure lid bolt bars.	Change reflects the current configuration for minimizing gap between SLB2 and closure lid. No impact to safety basis.
19	B-2/3	Added fillet weld callout for sealing Joloda rails to rear wall.	Weld callout eliminates potential virtual leak paths during leakage rate tests of metallic containment boundary, and reflects CTU-2 configuration. No impact to safety basis.

Summary of Changes, TRUPACT-III SAR DRAWING – 51199-SAR, Rev. 1			
Sheet	Zone	Change Description	Justification
19	B-7	CONTAINMENT STRUCTURAL ASSEMBLY: Changed Detail P to Detail AD.	Administrative change. No impact to safety basis.
19	C-7	CONTAINMENT STRUCTURAL ASSEMBLY: Updated view for rear SLB2 guide bars/plastic plate.	Change reflects the current configuration for minimizing gap between SLB2 and closure lid. No impact to safety basis.
19	C-8 D-7	CONTAINMENT STRUCTURAL ASSEMBLY: Changed to specific tolerances for CSA height and width from block tolerances.	Changes added tighter tolerances to reduce the potential movement of overpack cover relative to the CSA body. Improved safety basis.
20	B-7/8	Section AY-AY: Added missing double groove weld for joining the containment boundary plates.	Groove weld callout was missing from initial application. No impact to safety basis.
21	B-2	Changed Detail P to Detail AD.	Administrative change. No impact to safety basis.
21	B-7/8	Section L-L: Corrected view of bolt bars.	Administrative change. No impact to safety basis.
21	C-1 D-3	Detail AD: Changed liquid penetrant examination for weld joint from ASME NF to ASME NB.	Change reflects actual inspection criteria utilized for certification test units. No impact to safety basis.
21	C-2 C-3	Detail AD: Added missing fillet weld callout for attaching the front edge of Joloda rails to bottom floor plate.	Fillet weld callout was missing from initial application. No impact to safety basis.
21	C-4/5	Detail BE: Corrected section view of bolt bars.	Administrative change. No impact to safety basis.
21	C-6	Detail BE: Added "machine flat" callout and flag note 46 to groove weld that attaches bolt bar to front flange.	Change reflects actual configuration. No impact to safety basis.
21	D-5	Detail BE: Changed flange length dimension to reference dimension.	Change reflects actual configuration of the machined front flange face. No impact to safety basis.
21	D-4	Detail BE: Added GRIND FLUSH to CJP weld callout.	Change is required to allow fit-up of debris shield receptacle to the containment boundary. No impact to safety basis.
21	C-8 D-7/8	Section BN-BN: Corrected rear view of bolt bars.	Administrative change. No impact to safety basis.

Summary of Changes, TRUPACT-III SAR DRAWING – 51199-SAR, Rev. 1			
Sheet	Zone	Change Description	Justification
21	D-7	Section BN-BN: Changed liquid penetrant examination for weld joint from ASME NF to ASME NB.	Change reflects actual inspection criteria utilized for certification test units. No impact to safety basis.